Design Principles and Considerations for Spaceborne ATI SAR-Based Observations of Ocean Surface Velocity Vectors

Steffen Wollstadt, Paco López-Dekker, *Senior Member, IEEE*, Francesco De Zan, and Marwan Younis, *Senior Member, IEEE*

***Abstract*— This paper presents a methodology to design a spaceborne dual-beam along-track synthetic aperture radar interferometer to retrieve ocean surface velocity vectors. All related aspects and necessary tradeoffs are identified and discussed or reviewed, respectively. This includes a review of the measurement principle and the relation between baseline and sensitivity, the relation between wind and radar backscatter, a discussion of the observation geometry, including the antenna concept, polarization diversity, and all main error contributions. The design methodology consists of a sensitivity-based derivation of explicit instrument requirements from scientific requirements. In turn, this derivation is based on a statistical model for the interferometric phase error. This allows a quantitative, well-grounded instrument design offering an additional degree of freedom to the approach, which we call "noise-equivalent-sigma-zero requirement space." Crucial tradeoffs for the system design, such as the resolution, the number of independent looks, the minimum wind speed, and the coherence and ambiguities, are pointed out and discussed. Finally, this paper concludes with a single platform system concept operating in Ku-band, which provides the measurement quality needed to achieve a surface velocity estimation accuracy of 5 cm/s, 200-km swath coverage, for 4×4 km^2 L2-product resolution and winds starting at 3 m/s.**

***Index Terms*— Along-track interferometric (ATI), dual-beam interferometry, ocean surface velocity measurement, spaceborne mission design, synthetic aperture radar (SAR).**

I. Introduction

OCEAN surface currents are an important parameter in the understanding of climatic processes, ocean dynamics, and ocean–atmosphere interactions. In the last decades, there has been a significant progress in our understanding of oceanic processes. This has been the result of a combination of improved modeling, *in situ* measurement efforts, and enhanced remote sensing capabilities. By the intensive usage of scatterometry, altimetry, and radiometry, including the development and operation of spaceborne instruments and sensors, the knowledge about ocean wind, (geostrophic) currents, and sea surface temperature has been significantly increased on the basis of global coverage [1]. Also, several ocean products, such as, for example, the Ocean Surface Current Analyses Realtime (OSCAR), have been derived, allowing drawing conclusions regarding distinct ocean current contributions, such as Ekman and other ageostrophic constituents [2].

Despite the progress made in sensing and modeling ocean processes and, in particular, surface current features down to the mesoscale range (10–100 km), the direct measurement of ocean surface currents—especially in the submesoscale range (<10 km)—remains a clear observation gap. This gap needs to be filled in order to fully understand and model phenomena, such as air-sea fluxes of heat and momentum, or key vertical mixing processes, such as the vertical transfer of CO_2 and the transport of nutrients necessary to sustain marine ecosystems. Smaller scale processes tend to be more dynamic in nature. Consequently, achieving higher spatial resolution products naturally leads to a requirement for an improved temporal sampling.

So far, the retrieval of ocean currents from spaceborne measurements has been limited to *geostrophic* currents, which are derived from ocean topography maps obtained by altimeters. In order to achieve higher resolutions, wide swath ocean altimetry (WSOA) concepts that exploit cross-track synthetic aperture radar (SAR) interferometry have been introduced [3], [4]. A major milestone in WSOA will be the SWOT mission [5]. Over the last few decades, several research studies have evaluated the retrieval of ocean surface currents using along-track interferometric (ATI) data from airborne SAR systems [6]–[9]. It has been demonstrated that surface current velocities in the radar line-of-sight (LoS) map directly into the Doppler centroid of an SAR and the measured ATI phase provides an unbiased estimate of this Doppler centroid. It is, however, worth pointing out that, even in the absence of surface currents, significant Doppler centroids are observed that are linked to wave-motion, as discussed in Section II. These contributions need to be accounted for in the retrieval of ocean currents out of ATI or similar measurements, which is not within the scope of this paper.

The first ATI observations from space were obtained as a by-product of the Shuttle Radar Topography Mission (SRTM) [10], [11]. Although the SRTM baseline was primarily cross-track, it had a small along-track component, which was enough to demonstrate sensitivity to surface velocities. SRTM's hybrid

Manuscript received October 25, 2016; revised March 16, 2017; accepted March 28, 2017. This work was supported by the European Space Research and Technology Centre, European Space Agency, under Contract 4000109908/14/NL/BJ. *(Corresponding author: Steffen Wollstadt.)*

S. Wollstadt and M. Younis are with the Microwaves and Radar Institute, German Aerospace Center (DLR), 82234 Oberpfaffenhofen, Germany (e-mail: steffen.wollstadt@dlr.de).

P. López-Dekker is with the Department of Geoscience and Remote Sensing, Delft University of Technology, 2628 Delft, The Netherlands.

F. De Zan is with the Remote Sensing Technology Institute, German Aerospace Center (DLR), 82234 Oberpfaffenhofen, Germany.

Color versions of one or more of the figures in this paper are available online at http://ieeexplore.ieee.org.

Digital Object Identifier 10.1109/TGRS.2017.2692880

(cross- and along-track) baseline served as inspiration for some hybrid interferometry mission concepts [12]. It should be noted, however, that with a single hybrid baseline, it is impossible to separate the topographic from the velocity signatures. In order to go from a single surface velocity component in the LoS to 2-D vectors, the *dual-beam* system concept was introduced [13], [14]. The focus of this paper is the specification and design of spaceborne dual-beam ATI systems.

Starting from a set of mission requirements, the performance model presented is used to derive instrument requirements. This reveals a tradeoff space between sensitivity and nominal spatial resolution, which can be exploited to offer uniform product-level performance over a wide swath. Furthermore, all necessary geophysical and system aspects as well as considerations with respect to the measurement method are presented. While our reference mission scenario, discussed in Section VII, assumes a single-platform solution, the methodology and models used are also applicable to a formation flying concept.

This paper is structured in the following way. Section II presents the measurement concept, basic considerations on wind and current retrieval, and a comparison to a Doppler centroid anomaly (DCA) approach. Section III explains and reviews a number of fundamental issues to be addressed in the design of an ocean observing ATI SAR mission: acquisition geometry, baseline, polarization diversity, error contributions, and frequency band. Section IV presents the interferometric performance model used to derive the design process. Section V describes the instrument design procedure, emphasizing the tradeoffs that emerge in the process. Section VI gives an overview of the systematic errors, which have an impact on the ATI measurement. Finally, in Section VII, a system concept is presented, showing a feasible solution based on the methodology at hand.

II. Basic Concept and Velocity Measurement

A. Measurement Concept

The measurement concept is based on Dual-Beam along-track SAR Interferometry (DBI) [13]–[16]. An along-track SAR interferometer generates two SAR images acquired with almost the same geometry, but with a short time lag [17]. The ATI phase is given by

$$\phi_{\mathrm{ATI}} = 2\pi \frac{B_{\mathrm{AT}}}{\lambda} \cdot \frac{v_{\mathrm{r}}}{v_{\mathrm{orb}}} \tag{1}$$

where λ is the radar wavelength, v_{orb} the platform velocity, B_{AT} the physical along-track baseline, and v_{r} an effective Doppler velocity in the radial/LoS direction. In (1), we can identify the interferometric temporal lag as

$$\tau_{\mathrm{ATI}} = \frac{B_{\mathrm{AT}}}{2 \cdot v_{\mathrm{orb}}}. \tag{2}$$

Dividing the ATI phase by the time lag, and converting from radians to cycles, gives

$$f_{\mathrm{Dc}} = \frac{1}{2\pi} \cdot \frac{\phi_{\mathrm{ATI}}}{\tau_{\mathrm{ATI}}} = \frac{2 \cdot v_{\mathrm{r}}}{\lambda} \tag{3}$$

the well-known expression of the Doppler frequency.

For each point of the sea surface, there are several sources contributing to the Doppler velocity, including [18], [19]:

1) for Bragg scattering, the orbital velocity associated with the motion of gravity waves, and the phase velocity of the capillary waves;
2) for specular scattering, the group velocity of the wave packet;
3) for all scattering mechanisms, the mean surface velocity.

ATI (and DCA) measurements provide a spatial average of the sea surface motion projected in the LoS of the sensor weighted by the radar cross section (RCS) of each contributing scatterer. The normalized RCS (NRCS) of the ocean surface is modulated by the local slope, and statistically correlated with wave-related contributions to the local velocity. As a result, the NRCS-weighted mean velocity will be typically different from zero even when the average velocity is zero. From the point of view of mean surface velocity retrieval, this wave-related Doppler velocity contribution constitutes a geophysical bias. In summary, besides the desired mean surface velocity, the observed Doppler velocity depends strongly on the full sea state, which is dependent on ocean–atmosphere interactions, such as wind stress [18], [19].

In order to retrieve mean surface velocities, or surface currents, an inversion process is necessary that considers all contributions to the observed Doppler velocity [20]–[23]. Strictly speaking, even surface velocities and currents have to be distinguished, which implies also different inversion models. Assuming that an inversion process exists that eliminates the unwanted contributions to the velocity measurements, ocean surface currents can be derived from ATI SAR observations [11]. Since this paper concentrates on the system design, it will be assumed that this inversion process exists. Nevertheless, in the tradeoffs discussion, the necessity to facilitate this inversion will be considered.

As stated already, a DBI concept is assumed throughout the rest of this paper, using pairs of squinted antenna beams, one pointing in the fore-direction and the other in the aft-direction. In an ideal case, both LoS directions projected on-ground would be orthogonal to each other in order to obtain the same measurement sensitivity in all directions. However, as discussed in Section III-B, fixing a range-independent $\pm 45^{\circ}$ ground-projected squint, conflicts with other system design considerations.

B. On Surface Velocities and Wind

Although we focus on surface velocity retrieval, naively interpreting the ATI phase as a measurement of the surface velocity, we have to consider that the inversion process needs to jointly determine the sea state, which is closely linked to the surface wind [24], [25]. Insofar as the ATI measurement is sensitive to this surface wind, we need to have enough sensitivity in other observables (in particular in the NRCS) so that the sea-state or wind contribution can be estimated and inverted out. Current wind retrieval approaches are based on semiempirical relations, which are typically only valid or accurate for wind product resolutions in the order of tens of kilometers, at least an order of magnitude above the scientifically required product resolution for surface currents or velocities. We see this as one of the main challenges associated with the retrieval of accurate and high resolution surface velocities from measured Doppler velocities.

This full inversion process can be implemented in different ways but will always be supported by a geophysical model function (GMF). For wind-retrieval, the GMF accuracy mainly determines the geophysical inversion error (see Section III-C), which is typically in the order of 1.5 m/s, approximately 25% of the mean (global) wind speed [26]. Chapron *et al.* [18] showed validated models and measurements where the wind-related Doppler velocity amounts to around 20% of the wind speed. Combining these two findings suggests that a residual error of about 30 cm/s may be expected if the sea-state contribution is compensated based on conventional scatterometry. This is about one order of magnitude larger than the required precision of the final product, if a scientifically desired surface velocity accuracy of around 5 cm/s is assumed. In order to address this issue, consistent models are necessary as well as an (ideally) combined inversion and retrieval of all parameters, which is currently still a scientifically challenging task. Some data-based progress has been reported recently in [25]. In addition, there is some scientific evidence that the inversion process may be facilitated by the exploitation of polarization diversity. This is discussed in Section III-D.

Considering only the NRCS and viewing the system as a scatterometer, a dual-beam configuration will be sensitive to wind speed and direction, but greatly exposed to wind direction ambiguities. The scatterometric capabilities of the system may be improved in several ways, such as adding a third, unsquinted beam, in order to (at least) solve the typical 180° ambiguity. These techniques are exploited by spaceborne scatterometer missions, such as the Seasat-A Scatterometer System (SASS), the ERS-1/2 Scatterometer, the NASA Scatterometer (NSCAT), or European Space Agency's (ESA's) Advanced Scatterometer (ASCAT).

However, by exploiting the Doppler centroid information of the SAR measurement, the dual-beam concept should be sufficient to determine the surface winds from the backscatter information of the SAR measurements. Strictly speaking, the sign of the Doppler measurement can be used to solve the directional wind ambiguity. Therefore, an additional antenna beam is not found to be necessary. Direct wind vector retrieval from SAR measurements has already been investigated [27].

C. Concept Extensions

The system concept can be expanded in several ways in order to support the geophysical retrieval process. For example, the spaceborne platform could carry an additional altimeter, which would help to evaluate the coincidental ocean topography, which in turn is the main variable in order to determine the geostrophic current [19]. A drawback is that the altimeter (Nadir-looking) and SAR (side-looking) measurements do not cover the same area. The topography issue can also be solved by common cross-track interferometry. This idea has already been investigated, with an approach of combining along- and cross-track measurements [12], [28]. But, as already pointed out, it turned out that the interferometric phases due to the along- and cross-track baseline could not be separated or distinguished from each other, respectively [29]. A combined measurement would require an *additional*, spatially separated phase center and an appropriate baseline, which means a significantly increase in system size and cost.

D. Review of ATI Versus Doppler Centroid Measurements

Current, single-channel, SAR systems determine the Doppler velocity exploiting the DCA [18], [30]. In short, the DCA method estimates the difference between the centroid of the measured Doppler spectrum with respect to the expected (geometric) one. This difference is interpreted as an indication of the ocean surface velocity. ATI and DCA methods measure, in fact, the same geophysical quantity. Since—despite the abundant literature [8], [9], [21], [31]—there still seems to exist some confusion about it, this section provides an explicit comparison of both methods.

For this purpose, let us consider the Doppler spectrum of the radar echoes, $S_{\mathrm{D}}(f_{\mathrm{D}})$. This spectrum is given by the convolution of a geometrical Doppler spectrum, $S_{\mathrm{sys}}(f_{\mathrm{D}})$ and the Doppler spectrum of the scattering coefficient, $S_{\mathrm{scat}}(f_{\mathrm{D}})$

$$S_{\mathrm{D}}(f_{\mathrm{D}}) = \int S_{\mathrm{scat}}(\tilde{f}) \cdot S_{\mathrm{sys}}(f_{\mathrm{D}} - \tilde{f}) \cdot d\tilde{f}. \tag{4}$$

For example, for static surfaces, the spectrum of the scattering coefficient would only have zero frequency components, and would be the product of a Dirac-delta function times the NRCS of the surface, $\sigma_0 \cdot \delta(f_{\mathrm{D}})$. In general, power spectra form Fourier transform pairs with the corresponding autocorrelation functions. Since a convolution in the frequency domain corresponds to a product in the time domain, we have

$$R_{\mathrm{D}}(\tau) = R_{\mathrm{scat}}(\tau) \cdot R_{\mathrm{sys}}(\tau). \tag{5}$$

The central moments of a power spectrum, $S(f)$, can be written in terms of the autocorrelation function, $R(\tau)$, and its derivatives evaluated at $\tau = 0$ [32]. In particular, the zeroth moment is simply

$$\int_{-\infty}^{\infty} S(f) \cdot df = R(0) \tag{6}$$

and the first moment is given by

$$\int_{-\infty}^{\infty} f \cdot S(f) \cdot df = \frac{-j}{2\pi} \frac{dR(\tau)}{d\tau}\bigg|_{\tau = 0}. \tag{7}$$

In order to evaluate the right-hand side term in (6), we write the autocorrelation function in polar form: $R(\tau) = A(\tau)e^{j\cdot\phi(\tau)}$. From the fact that an autocorrelation has always a real-valued maximum at the origin, it follows that $A'(0) = 0$. Consequently, after applying the chain rule, the time-derivative of the autocorrelation function at the origin reduces to

$$\frac{dR(\tau)}{d\tau}\bigg|_{\tau = 0} = j\,\frac{d\phi(\tau)}{d\tau}\bigg|_{\tau = 0} \cdot R(0) \tag{8}$$

and the power-normalized first moment, or centroid, of the power spectrum is given by

$$f_{\mathrm{c}} = \frac{\int_{-\infty}^{\infty} f \cdot S(f) \cdot df}{R(0)} = \frac{1}{2\pi} \frac{d\phi(\tau)}{d\tau}\bigg|_{\tau = 0}. \tag{9}$$

Applying the chain rule to (5) and applying the previous results, the Doppler centroid of the Doppler spectrum of the radar echoes can be written as

$$f_{\mathrm{Dc}} = \frac{1}{2\pi}\frac{d\phi_{\mathrm{scat}}(\tau)}{d\tau}\bigg|_{\tau=0} + \frac{1}{2\pi}\frac{d\phi_{\mathrm{sys}}(\tau)}{d\tau}\bigg|_{\tau=0} = f_{\mathrm{Dc,scat}} + f_{\mathrm{Dc,sys}}. \tag{10}$$

The second contribution is the system, or geometric, Doppler centroid, and it is given by [33]

$$f_{\mathrm{Dc,sys}} = \frac{1}{2\pi}\frac{d\phi}{dt} = \frac{2v_{\mathrm{orb}}}{\lambda}\sin(\theta_{\mathrm{s}}) \tag{11}$$

which takes only system parameters into account: the satellite velocity v_{orb}, and the squint angle θ_{s}. The first term is the DCA.

Turning now our attention to the ATI case, we can identify in the complex valued and multilooked interferogram an estimate of the temporal autocorrelation function of the scattering coefficient

$$R_{\mathrm{scat}}(\tau) = E\{s(t+\tau)s^*(\mathrm{t})\} \tag{12}$$

evaluated at the temporal lag $\tau = \tau_{\mathrm{ATI}}$, where $E\{\cdot\}$ denotes the expected value operator. The interferometric phase for small values of τ_{ATI} can be approximated by its first-order Mclaurin series expansion

$$\phi_{\mathrm{ATI}} \approx \frac{d\phi_{\mathrm{scat}}(\tau)}{d\tau}\bigg|_{\tau=0} \cdot \tau_{\mathrm{ATI}}. \tag{13}$$

Substituting in (3), shows that the Doppler frequency estimated from the ATI measurement is indeed the same as the DCA as long as the ATI lag is small. As criterion for small enough, we can take that τ_{ATI} should be small compared with the coherence time of the surface.

The accuracy with which the DCA can be determined is dependent on the geometric Doppler centroid accuracy following from the satellite attitude knowledge, and on the Doppler centroid estimation accuracy [30]. DCA methods require well-characterized antenna patterns (which map directly into well-characterized Doppler spectra) with well-defined peaks. As a consequence, DCA techniques are incompatible with ScanSAR modes, and also do not perform well in combination with a TOPS acquisition mode. The clear advantage of this method is that it is compatible with any traditional, single-antenna, SAR system. It is worth noting that DCA performance improves as the length of the antenna increases.

The key advantages of ATI are as follows.

1) For the same power and total antenna size, ATI provides much better sensitivity. This higher intrinsic sensitivity can be used, for example, to provide higher resolution products, or to relax system requirements. Based on the investigations of real data sets, this has also been argued by Kersten *et al.* [34] and particularly in the case of a required higher spatial resolution by Romeiser *et al.* [35].
2) ATI does not impose stringent restrictions on the antenna pattern, and is compatible, for example, with any kind of burst imaging mode.
3) As it will be shown in Section III, for *short* baselines, the required sensitivity is inversely proportional to the baseline: increasing the baseline by a factor of two is equivalent to increasing the transmit power by a factor 4 (6 dB). This performance improving mechanism does not have an equivalent in the case of DCA.

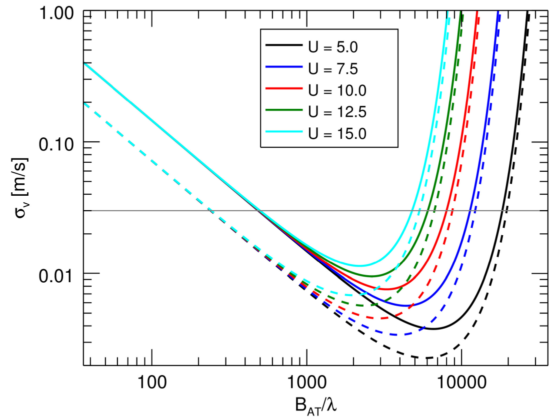

Fig. 1. Standard deviation of the (radial, on-ground projected) Doppler velocity as a function of the one-way baseline, normalized by the wavelength, for different wind speeds, 30° incident angle, 4000×4000 m^2 product resolution with 160 000 looks, and SNR levels of 0 dB (solid lines) and 5 dB (dashed lines) for an LEO. The horizontal line denotes a desirable error of 3 cm/s.

III. Principal Considerations

The presented topics in this section are fundamental for a full comprehension and development of an ATI SAR-based ocean surface velocity measurement system.

A. Optimal ATI Baseline

One of the most important parameters in an ATI mission is the along-track baseline. As shown by (1), the sensitivity to Doppler velocities scales with the baseline. However, longer baselines also imply a higher degree of temporal decorrelation. The optimum along-track baseline depends through several mechanisms on the sea state, the radiometric sensitivity of the system, and the observation geometry. This baseline dependence is shown in Fig. 1 for low Earth orbit (LEO) systems, where the LoS velocity error is shown as a function of the (physical) along-track baseline for different wind velocities and two signal-to-noise ratio (SNR) levels [36].[1] Note that the baseline is expressed in wavelengths in contrast to related illustrations, for example [37], in order to find an optimum baseline for any system wavelength. A product resolution of 4000×4000 m^2 has been assumed for a nominal single-look resolution of 10×10 m^2, which results in 16×10^4 independent looks.

In order to quantify the amount of temporal decorrelation, we assume the derivation originally made by Tucker [38], in a form presented in [14]. There, the Pierson–Moskowitz sea spectrum [39] is used, and integrated in an interval of relevant frequencies to calculate the variance of the radial velocity component, $\sigma^2_{v_{\mathrm{r}}}$. The standard deviation of the Doppler

[1]The calculation of the error is based on the model, which is derived in detail later in Section IV-A.

frequencies, which can be interpreted as a Doppler bandwidth, is then given by

$$\Delta f_{\mathrm{D}} = \sigma_{f_{\mathrm{D}}} = \frac{2}{\lambda} \cdot \sigma_{v_{\mathrm{r}}}. \tag{14}$$

The coherence time is then the inverse of this Doppler bandwidth, and given by

$$\tau_{\mathrm{c}} = \frac{1}{\Delta f_{\mathrm{D}}} \approx 3.29\frac{\lambda}{U}\mathrm{erf}^{-0.5}\left(2.688\frac{\rho}{U^2}\right) \tag{15}$$

where U is the wind speed at a reference height, and ρ is the resolution. The choice of ρ is somewhat problematic and a common source of confusion. For the ATI performance analysis, we must consider the multilooking process, which is averaging phases, or velocities, over the scales given by the product resolution. Therefore, for the ATI quality, what matters is this multilooked product resolution. For ρ coarser than 100 m, this coherence time can be approximated by $\tau_{\mathrm{c}} \approx 3.29\lambda/U$. It is furthermore important to mention that the derivation of (15) ignores the NRCS weighting of the different velocities. As already discussed, this weighting skews the distribution of Doppler velocities measured by the radar. This leads to geophysical biases, but also to narrower distributions, smaller variances, and, consequently, longer coherence times. For the purpose of this paper, however, (15) is taken as a conservative assumption.

Qualitatively, it can be observed in Fig. 1 how the optimum baseline shifts toward smaller values for higher winds (larger ocean waves) and better SNRs. In practice, a compromise value needs to be found suitable for a range of sea-state conditions. According to Fig. 1, as a rule of thumb, a range of physical ATI baselines of 1000λ–2000λ appears to be the optimum. This implies optimal baselines around 50 and 100 m at X-band and C-band, respectively, which is consistent with results found in the literature [21]. It also shows that the baseline of a single platform system for Doppler velocity measurement will always be shorter than the ideally proposed optimum, which yields still a baseline of 22–44 m in the Ku-band case. For a single platform system design with a smaller baseline, one has to consider a lower baseline limit, where the error is below a reasonable threshold. For example, this is approximately 500λ in Fig. 1 for a 3-cm/s error at 0-dB SNR.

B. Observation Geometry and Antenna Concept

The following paragraphs discuss tradeoffs around the observation geometry, which is closely related to the antenna concept. A driving parameter is the desired temporal and spatial coverage of the Earth, i.e., the repeat cycle and the swath width. There are a number of fundamental design choices to be made.

1) Electronic Versus Mechanical Azimuth Beam Steering: The natural option to implement arbitrarily pointed antenna patterns is to do it mechanically, as it is done in airborne DBI systems. In a spaceborne scenario, however, considering the deployment of the antennas, solutions allowing the use of linear antennas, aligned in the direction of flight, is preferable. This can be implemented as a phased array, or using leaky waveguide concepts, for example. We refer to this linear system structure as a *javelin* solution (see, for example, Fig. 14).

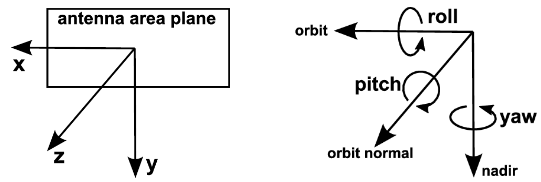

(a) (b)

Fig. 2. Coordinate systems for describing the antenna steering. (a) Antenna system (x-axis aligned with orbit/flight direction). (b) Nadir oriented system defining yaw, pitch, and roll angle.

Using an aperture aligned with the flight direction, instead of a mechanically pointed one, has some implications with regard to the resulting antenna footprint on-ground, which is independent of the antenna hardware realization. For example, the patterns can be calculated, without loss of generality, assuming an electronically steered phased array. In order to understand the differences between both solutions, we compare both beam-steering concepts for an intuitive and typical azimuth beam-steering case. We take a look to the antenna rotation order with respect to two coordinate axes: the electronic steering, in the case of a typical javelin antenna mounting, inherits first a roll-steering of the antenna and then a rotation around the y-axis of the antenna aperture plane, where the latter rotation is done electronically by applying a linear phase to the array elements. But if we consider the, maybe, most intuitively mechanical antenna mounting for the azimuth squinted case, the first rotation in the mechanical steering is a yaw-steering of the antenna and then a rotation around the x-axis in the antenna aperture plane (see coordinate systems in Fig. 2). Therefore, the resulting footprints are different as shown in Fig. 3. However, any electronic beam-steering with its corresponding footprint can be emulated by appropriate mechanical rotations of the antenna. But a system designer has to be aware of the implications of his beam-steering concept with respect to the resulting footprint shape on-ground.

Furthermore, the different footprint shapes yield a difference in the incident angles and the squint angles on-ground. The advantage of the shape in Fig. 3(a) is the smaller incident angle range, since the mechanical, more tilted pattern has to be "longer" to cover the same swath in elevation. A 200-km swath yields a range of, for example, 26°–36° [see Fig. 15(a)], whereas the mechanical steering case requires 22°–40°. These results in a smaller receive echo window length and therefore larger possible pulse repetition frequencies (PRFs) in order to improve the azimuth ambiguity performance. On the contrary, the advantage of the shape in Fig. 3(b) is the constant squint angle on-ground, which has an impact on the sensitivity of the product performance.

It can be shown that the phased-arraylike pattern follows an iso-Doppler line of its corresponding squint angle [see Fig. 3(a)]. The elevation sidelobes are also on the same iso-Doppler line. A positive consequence of this is that the Nadir direction, which corresponds to a zero Doppler, will not be illuminated by an elevation sidelobe as it is the case for a conventional zero-Doppler acquisition. In other words, the Nadir position is outside the main azimuth and main elevation

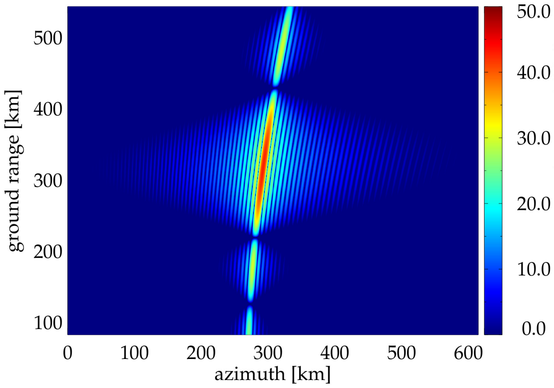

(a) Electronic antenna steering

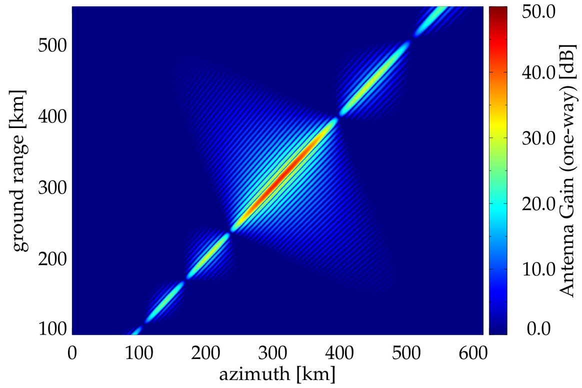

(b) Mechanical antenna steering

Fig. 3. Antenna pattern projected on-ground covering a subswath of ∼60 km with an antenna size of 3.6 × 0.2 m^2 in an LEO. (a) Phased-array antenna with an electronic steering of 18.5° in azimuth, resulting in a squint angle on-ground of approximately 40° to 45°. (b) Antenna with a (typical) mechanical steering (tilting) in azimuth of 45°.

sidelobes of the 2-D pattern, which results in a very strong Nadir-suppression by the antenna pattern, which simplifies the timing and swath coverage design.

A drawback of electronically beam-steered antennas regarding instrument size and weight is the need to be physically larger than mechanically tilted ones for prescribed beamwidths. The reason is that the effective aperture in the direction of the beam is smaller than the physical aperture. This effect is approximately described by a length-scaling factor of $\cos(\theta_s)$, where θ_s is the squint angle. A quite large squint angle of 18° yields a decrease of the effective aperture of around 5%.

2) Single Versus Two Side-Looking Concept: Obviously, a system looking left *and* right gathers twice as much information as a single side-looking system. However, our intention is the tradeoff between different systems covering the *same* swath size. This leads to a dependence on the incident angle range. The single side-looking concept yields a much larger incident angle variation in order to obtain the same coverage like the version looking to both sides. The latter concept results in two equal incident angle ranges, each having a smaller variation, and implies also a gap in-between, which means a noncontinuous swath coverage in elevation around the subsatellite track. If incident angles in far range were to be favored, one can nevertheless design a two side-looking implementation, accepting a larger gap at nadir between both swaths. Concerning the instrument hardware, a single side-looking concept is preferred due to thermal issues, for instance.

3) Incident Angle Range (and Orbit Height): The incident angle range plays an important role for the system performance. Staying in near range and steeper incident angles, where the backscattered power is much higher, makes it easier to provide the required SNR. In fact, in a naive design process that considers only the pure interferometric performance, including the deprojection from LoS to horizontal velocities, but ignoring the overall inversion process and all sources of bias, leads to solutions with very steep incident angles. There are, however, the following strong motivations to choose larger incident angles.

1) Far range geometry provides a better projection of the horizontal velocities in the LoS, which reduces the impact of systematic errors.
2) The scatterometric sensitivity to wind speed and direction is much stronger in far range, which is paramount for a good joint inversion process.
3) The polarimetric signature is also much more clear at larger incident angles.
4) The relative weight of geophysical biases is smaller. This is because vertical and horizontal components of the orbital wave-velocities are equal for circular motions associated with deep water, so that the geophysical biases in the LoS Doppler velocities are more or less incident angle independent, while the sensitivity to mean horizontal motions is not.

Therefore, a general mission design rule is to choose a range of incident angles as much in far range as possible within the available (sensitivity) resources.

Furthermore, the incident angle range is directly related to the orbit height. A lower orbit improves the sensitivity of the system, but a higher orbit decreases the incident angle range (assuming the same swath width). This means the incident angle variation is less, which in turn decreases the variation of the elevation performance (across the swath). Besides the performance aspects, also system considerations have shown that the disadvantages of the higher orbit, such as a larger power consumption, may be compensated by a reduced eclipse duration and an increased downlink time, for instance.

C. Total Error Contributions

Dealing with mission and instrument design implies dealing with errors or minimizing them, respectively. This section characterizes the main error sources in an ocean surface velocity measurement mission.

1) System Noise: The instrument related thermal white noise is the usually best understood source of error. The interferometric surface velocity error depends on the SNR and the number of independent looks, so that it can be only mitigated by improving the instrument performance in terms

This article has been accepted for inclusion in a future issue of this journal. Content is final as presented, with the exception of pagination.

of sensitivity and resolution, or by increasing the baseline. The measurement noise and its impact is (indirectly) the subject of Sections IV and V, since it is the basis of our system design methodology.

2) Geophysical Noise: This can be described as random errors intrinsically associated with the stochastic nature of the ocean surface. For example, waves induce random motions resulting in local variations of the instantaneous surface velocity that need to be averaged out. The scales of these variations, or more generally speaking their 2-D wave spectra, are sea-state-dependent, since waves grow longer for larger winds, and determine the spatial scales over which the measurements need to be averaged. A consequence is that for a given target resolution, there is a minimum sea-state-dependent measurement uncertainty, which is independent of the instrument itself. The geophysical noise is considered to some extent by the applied multilooking factor, but there remains the measurement uncertainty explained earlier, since the averaging is only appropriate for some local surface variations.

3) Instrument Related Systematic Errors: These are caused by unknown phase offsets resulting from receiver electronics or other microwave components, and by uncertainties in the exact relative position of the receive antennas with respect to the spacecraft trajectory. These position uncertainties can be caused by either attitude knowledge errors, thermoelastic deformations, or structural oscillations. The systematic instrument errors require a separate evaluation, which is performed in Section VI.

4) Geophysical Inversion Errors: These are inversion biases, ultimately caused by an imperfect or oversimplified modeling of the relation between the observables (σ_0 and ATI phases for the different beams and polarizations) and the geophysical variables of interest, and by the fact that the number of observables is smaller than the number of geophysical variables determining them. This implies that the inversion models need to make assumptions, which are not always correct. For ocean velocity and current estimation, the largest contribution to the inversion error is caused by uncertainties in the wind-wave spectrum, describing the insufficient knowledge of the ocean state, and their contributions to the (wave-motion related) effective Doppler velocity (see Section II-A). This is also the main reason why simultaneous retrieval of wind and currents is essential. Finally, the geophysical biases, actually considered as the major error source in the final product, are not part of this system-based design, but have obviously to be considered in an accuracy budget of an end-to-end surface current retrieval analysis.

D. Polarization Diversity

The application of polarization diversity is considered as an important step in order to improve the geophysical inversion error (see Sections II-B and III-C). Following [40], the NRCS of the ocean can be decomposed into three main components: Bragg scattering, specular scattering, and contributions from breaking waves. Investigations on polarimetric data have shown that polarization diversity can support the distinguishing of Bragg scattering (which is polarized) from wave breaking (nonpolarized), which can have a significant contribution to the total NRCS [41]. The Doppler velocity component associated with the mean surface velocity is purely geometric and, hence, polarization-independent. In contrast, the wave-motion related effective Doppler shift depends on the polarization [18], [24]. These issues are confirmed by several more recent studies [42], [43]. Considering the second order statistics, a single-polarized instrument delivers, for each direction, a 2×2 covariance matrix characterized by three real-valued, independent observables: the intensity, and the amplitude and phase of the interferometric coherence. A hybrid or dual polarized system yields 4×4 covariance matrices, with two real-valued intensities, and four independent complex-valued terms. It must be considered, at the very least, scientifically plausible that the inversion process will benefit from this enlarged observation space.

This reasoning would speak in favor of a fully polarized solution. Under most conditions, however, the cross-polarized return is around 13–18 dB below the copolarized component [44], and too weak to be exploited. Therefore, the additional cost, complexity, and data volumes associated with a quad-pol solution can hardly be justified. This leaves a dual-pol and a hybrid-pol option, which can be implemented as 45° linear or a circular solution. In agreement with some studies, we consider a hybrid-polarized solution [45], with circular polarization on transmit and linear polarization on receive, as the best compromise solution. An additional advantage is the rotational invariance to the illumination, particularly in the context of a strongly squinted geometry. It simplifies the system and antenna design, since the radiated energy is always equally distributed on-ground between horizontal and vertical polarizations.

For our performance analysis, we assume that the cross-polar return is negligible, treating the hybrid solution, in essence, as an equivalent dual copolarized system. The required polarization reconstruction necessary due to the azimuth squinted beams is derived later in this paper. However, the importance of cross polarization for the inversion becomes more significant for strong wind conditions, therefore further investigations on this issue are recommended to be carried out.

E. Frequency Band

The choice of operating frequency band is driven by a mix of technological and geophysical (retrieval-related) reasons. For single-platform solutions, only high frequency bands, such as Ka (and Ku), allow approaching the optimum baseline of 1000–2000 wavelengths. Higher frequency bands are also favorable in terms of instrument and antenna sizes. On the other hand, it is quite well known that high frequency bands, such as Ka-band, are affected by significantly higher atmospheric attenuation, in particular in the presence of precipitation. From the point of view of the geophysical surface velocity retrieval, according to the recommendation of [21], although maybe not obvious, the relevance of a high radar frequency increases with the strength of the current gradients to be imaged, with wind speed, and with the spatial resolution of the radar and the required accuracy. Nevertheless, current fields (with small and slow changing gradients) have also been extracted successfully from the L-band data [8]. The maturity from a technological point of view could be a practical limitation and an indication for lower bands, such as L-band, C-band, or X-band. The necessary baseline-related sensitivity for lower bands could be achieved by means of a formation flying system. However, the approach presented in this paper can be applied to each system independent of the applied radar frequency.

IV. Derivation of Interferometric Performance

The main parameter for the instrument design is the requirement on the error of the surface velocity. Due to its random nature, here, we essentially consider the measurement error in our methodology (see Section III-C). The evaluation of this error is called interferometric performance or (L2-)product performance, respectively.

A. Interferometric Performance Model

The standard deviation of the surface velocity is used as a direct indicator of the estimation accuracy.[2] The relation between the interferometric phase and (radial) surface velocity, after deprojection on the ground is

$$v_{\mathrm{r,p}} = \frac{\lambda}{4\pi} \cdot \frac{\phi_{\mathrm{ATI}}}{\tau_{\mathrm{ATI}}} \cdot \frac{1}{\sin(\theta_{\mathrm{i}})} \tag{16}$$

where θ_{i} is the incident angle. Now we use the Cramer–Rao lower bound (CRLB) for the phase standard deviation [46]

$$\sigma_{\phi_{\mathrm{ATI}}} = \sqrt{\frac{1-\gamma^2}{2N_{\mathrm{l}}\gamma^2}} \tag{17}$$

where γ is the coherence and N_{l} is the number of independent samples. Therefore, the performance along the on-ground projected LoS, i.e., the standard deviation of the surface velocity can be modeled by using (16) and (17)

$$\sigma_{v_{\mathrm{r,p}}} = \frac{1}{\sin(\theta_{\mathrm{i}})} \frac{\lambda}{4\pi} \sqrt{\frac{1-\gamma^2}{2N_{\mathrm{l}}\gamma^2}} \frac{1}{\tau_{\mathrm{ATI}}}. \tag{18}$$

One can observe that the surface velocity performance is strongly dependent on the coherence and the number of independent looks. A similar approach for modeling the surface velocity error has been applied by Moller *et al.* [47].

B. Validity of Performance Model

The performance model for the surface velocity error (18) assumes that the CRLB, as derived in [46] and [48] is correct. Although this bound is used quite often to obtain an estimate of the interferometric measurement uncertainty, it is worth to reflect on the assumptions made in the derivation of this CRLB. One of the main ones is that the complex radar signal is statistically homogeneous (stationary in the spatial domain), with each complex value being drawn from a circular-Gaussian distribution [49], which in turn results in a Rayleigh-distributed amplitude.

There is an abundance of literature on the statistical characterization of sea-clutter [50]–[52], as the issue is of great relevance in the context of target detection. Radar scattering of the ocean surface can be reasonably well described as a two-scale compound-process [53], where fully developed circular-Gaussian speckle at smaller scales is modulated in amplitude by the slopes resulting from larger scale gravity waves. These slopes are also random in nature. In addition, there are contributions from scattering of breaking waves, which are important at near-grazing angles, and of specular scattering, which are dominant at very steep angles of incidence. A common model used to describe sea-clutter statistics is the K-distribution [54]. The K-distribution is characterized by a shape parameter, ν, that controls the length of the tail of the amplitude distribution. Smaller values correspond to *spikier* distributions with longer tails. The shape parameter depends strongly on the observation geometry and the sea state. According to [55], generally the values of ν range from 2.5 to ∞. From [56], it can be seen that for large incident angles of around 45° (still of interest for an SAR mission), values of 4–20 can be assumed.

In order check the validity of the CRLB, numerical simulations have been carried out, generating interferometric data sets assuming a pure circular-Gaussian distribution or a K-distribution, respectively. The simulation code is available online [57]. Fig. 4 shows the numerically estimated phase uncertainty, normalized with the number of looks ($\sigma_\phi \cdot \sqrt{N_{\mathrm{l}}}$), as a function of SNR for circular-Gaussian signals and for K-distributed signals with shape parameters ranging from 1 to 8. Two levels of temporal decorrelation have been

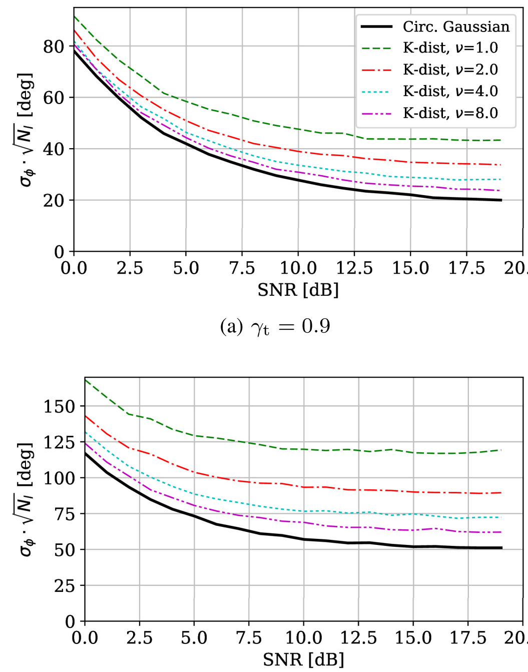

(a) $\gamma_{\mathrm{t}} = 0.9$

(b) $\gamma_{\mathrm{t}} = 0.5$

Fig. 4. Comparison of the phase error for a pure circular-Gaussian sea-clutter signal model and a K-distributed model for various values of the shape parameter. The phase errors are normalized with the number of looks, and shown as a function of SNR. (a) corresponds to a case with low temporal decorrelation, which is representative for a single-platform solution. (b) assumes a significant decorrelation ($\gamma_{\mathrm{t}} = 0.5$), which could be encountered in a formation-flying case.

[2]This assumes the existence of an inversion algorithm capable of separating the different velocity components of the observed Doppler velocity, as discussed in Section II.

This article has been accepted for inclusion in a future issue of this journal. Content is final as presented, with the exception of pagination.

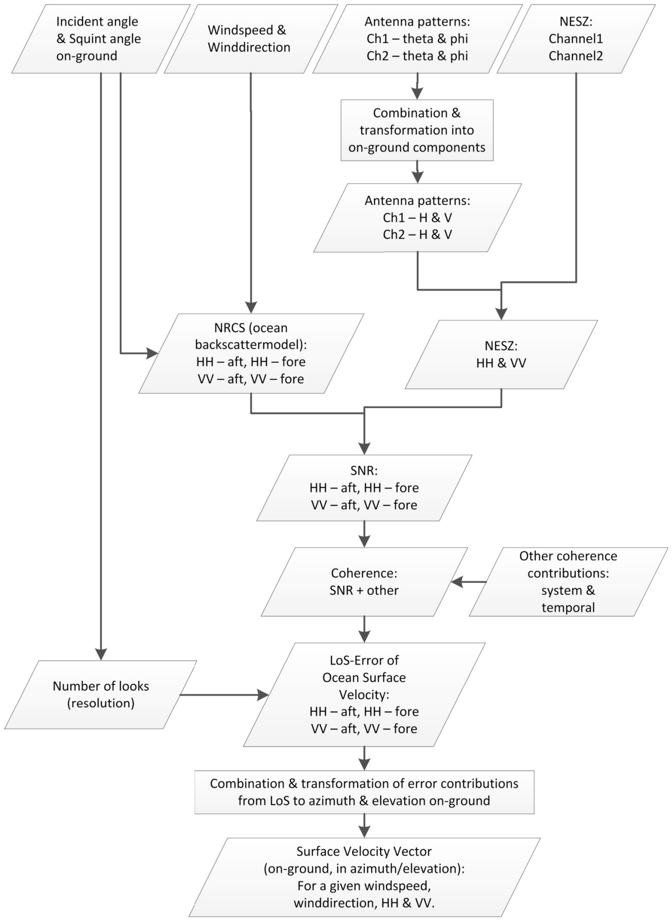

Fig. 5. Flowchart of interferometric performance evaluation.

considered. Fig. 4(a) assumes a temporal decorrelation factor of $\gamma_t = 0.9$, which we may consider representative of a single-platform solution. Fig. 4(b) assumes a factor $\gamma_t = 0.5$, which could be consistent with a formation-flying configuration. In both cases, the main conclusion is that for shape parameters above 4, the phase uncertainty for the K-distributed case is very close to the circular-Gaussian one. Therefore, it may be concluded that the CRLB given by (17) may be, indeed, used.

C. Methodology

In order to derive the interferometric performance, we basically have to evaluate (18) for each LoS (fore and aft) separately and then perform the combination of the results to obtain the 2-D error. An overview of the overall calculation is shown in the flowchart in Fig. 5. It starts with the outputs of the SAR performance calculation and ends in the 2-D standard deviation of the surface velocity. In order to simplify the explanation of the evaluation flow, it shall be broken down into six main steps, which are discussed in the following. Note that we use throughout the explanation parameters of our final instrument concept in Section VII for a better illustration.

1) Inputs/SAR Performance Outputs: According to Fig. 5, four inputs are required, which are output of SAR performance calculations [33]: the acquisition geometry, namely, the incident angle and squint angle on-ground (see Section III-B), the antenna patterns, the noise-equivalent-sigma-zero (NESZ) of the instrument, and finally, the wind speed and direction.

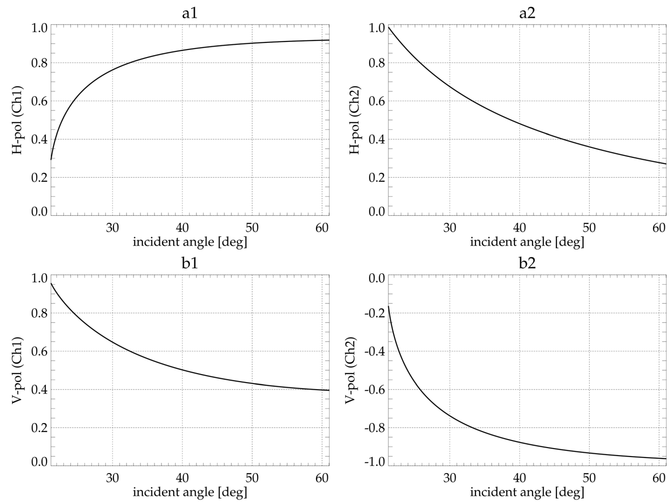

Fig. 6. Geometric polarization factors a_1, a_2, b_1, and b_2 (range position-dependent) due to a 18.5° squinted geometry using a phased-array antenna: describing the relation between the electric fields of each channel and the target area polarization (on-ground) over a large incident angle range of 20°–60° (approximately 1000-km ground range). The y-axis of, e.g., factor "a1" describes the contribution of channel 1 to the horizontal polarization on-ground. The Euclidean norm of "a1" and "a2" describes the total available horizontal polarized energy, whereas the norm of "a1" and "b1" provides the full energy transmitted by channel 1 (and vice versa). For details, see Appendix A.

2) Polarization and NESZ Reconstruction: We assume that some kind of dual, compact, or hybrid polarization is used, as discussed in Section III-D and recommended in [18]. Therefore, each of the two instrument look directions needs an antenna configuration with two channels for transmit (Tx) and receive (Rx) having orthogonal polarizations. According to Section III-B, we can apply two different squint mechanisms to obtain the dual-beam system. For the (*mechanical*) one generating the footprint in Fig. 3(b), the following polarization reconstruction is not necessary. But, the favored (*electronic*) one, generating the footprint along an iso-Doppler line [see Fig. 3(a)], requires the following considerations.

From an antenna-engineering point of view, it is common to tag the polarizations following the orientation of the electrical fields at the aperture. The two resulting orthogonally polarized waves (here, referred to as channels 1 and 2) do not correspond necessarily to horizontal (H) and vertical (V) polarizations on the illuminated surface [14], [47], since the H polarization is defined as the electric field vector normal to the incident plane and the V polarization as the vector parallel to the incident plane, always with respect to the illuminated ground. This polarization mixing is dependent on the incident angle. For an unsquinted or mechanically rotated antenna, these antenna polarizations coincide with the polarizations of the electromagnetic wave on the ground.

Therefore, a reconstruction of the polarization from the two antenna channels is required. The relation of the electric fields of each channel and each polarization on-ground can be described by a factor (depending on the incident angle). These *geometric polarization factors* are shown in Fig. 6, exemplarily for an LEO and a squint angle of 18.5°. A detailed derivation is presented in Appendix A. With these polarization

This article has been accepted for inclusion in a future issue of this journal. Content is final as presented, with the exception of pagination.

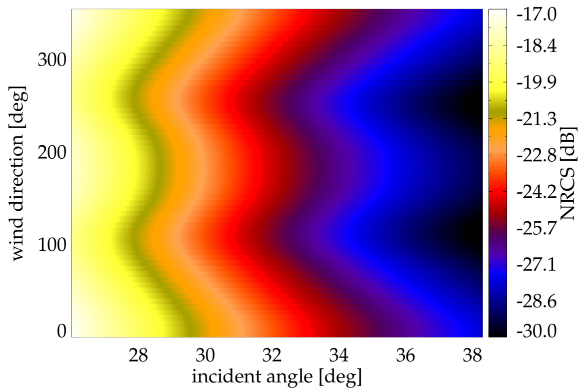

Fig. 7. Ocean NRCS values in dB for a wind speed of 2 m/s and VV polarization; based on NSCAT-3 GMF.

factors, the reconstruction of the desired scattering polarization coefficients related to Tx and Rx ("HH" and "VV") is possible. A description of the reconstruction is given in Appendix B.

Finally, we have to transfer this reconstruction to the NESZ in our performance calculation. This procedure is described in Appendix C. The resulting polarization-dependent NESZ can be finally used for the evaluation of the SNR or γ_{SNR}, respectively.

3) Backscattermodel and Surface Wind: The subsequent SNR calculation in Fig. 5 requires, additionally to the NESZ, NRCS values of the target area. Several backscattering models from scatterometer SAR missions are available in order to provide (wind-based) NRCS values, for example, the NSCAT GMF [58] or the SASS (Seasat-A) GMF [59]. The GMFs are dependent on incident angle and surface wind, i.e., speed and direction. Fig. 7 shows the NRCS values for a wind speed of 2 m/s. For such low wind speeds, the NRCS is also very low with -30 to -17 dB. For higher wind speeds, the backscatter is much stronger (up to 3 dB at 10 m/s) and has a stronger signature regarding incident angle and wind direction. Therefore, low wind speeds are the worst case for the interferometric performance calculation. Note that we need to extract 2×2 sets of NRCS values, two for the look directions (fore and aft) as well as for both polarizations.

4) Coherence and SNR: After retrieval of the NRCS values and the NESZ evaluation for both polarizations, the next step in Fig. 5 is calculating the four SNR values (fore/aft and H/V)

$$\mathrm{SNR}(\theta_{\mathrm{s}}, p) = \frac{\sigma^0(\theta_{\mathrm{s}}, p)}{\mathrm{NESZ}(p)} \tag{19}$$

where σ^0 represents the NRCS, p represents the polarization (H/V), and θ_{s} represents the squint angle in order to indicate the fore- or aft-looking direction. This is an intermediate step in order to estimate the overall coherence, which can be described by the well-known partial coherence multiplication rule

$$\gamma \approx \gamma_{\mathrm{SNR}} \cdot \gamma_{\mathrm{t}} \cdot \gamma_{\mathrm{sys}} \tag{20}$$

where γ_{SNR} is the remaining coherence due to noise, γ_{t} is the coherence due to temporal decorrelation, and γ_{sys} describes the system coherence. All SNR contributions can be translated into coherence values by

$$\gamma_{\mathrm{SNR}} = 1/(1 + \mathrm{SNR}^{-1}). \tag{21}$$

The temporal decorrelation in (20) can be considered by

$$\gamma_{\mathrm{t}} = \exp\left(-\tau_{\mathrm{ATI}}^2/\tau_{\mathrm{c}}^2\right) \tag{22}$$

where τ_{c} is the coherence time given in (15) and τ_{ATI} is the temporal baseline lag (2). The system coherence γ_{sys} in (20) comprises basically the decorrelation due to ambiguities and quantization. The ambiguity coherence γ_{amb} can be calculated by means of the azimuth and range ambiguity ratios or the distributed-target-ambiguity-ratio (DTAR), respectively

$$\gamma_{\mathrm{amb}} = 1/(1 + \mathrm{DTAR}). \tag{23}$$

The quantization coherence γ_{quant} depends on the number of quantization bits. A sufficiently high quantization, e.g., 4-bit, should already yield a very good coherence of 0.99 [60]. A 3-bit quantization coherence of 0.966 is a too low requirement for the application at hand.

5) Number of Looks and Resolution: The number of independent looks N_{l} or samples, respectively, is a measure for the averaging of the resulting product resolution. It is the ratio of product resolution ρ_{L2} and nominal geometric resolution $\rho_{\mathrm{2\text{-}D}}$

$$N_{\mathrm{l}} = \rho_{\mathrm{L2}}/\rho_{\mathrm{2D}}. \tag{24}$$

Note that the smearing due to temporal decorrelation does not change the number of looks. It depends only on the *nominal* resolution. The 2-D resolution is the product of range and azimuth resolution and can be calculated by

$$\rho_{\mathrm{2D}} = \frac{\rho_{\mathrm{rg}} \cdot \rho_{\mathrm{az}}}{\cos(\theta_{\mathrm{sg}})} \tag{25}$$

where ρ_{rg} is the slant range, ρ_{az} is the azimuth resolution, and θ_{sg} the squint angle projected on-ground. In the ScanSAR imaging case, the (swath-dependent) resolution is approximately

$$\rho_{\mathrm{2D}}(n_{\mathrm{s}}) \approx \frac{c_0}{2W_{\mathrm{rg}}(n_{\mathrm{s}})\sin(\theta_{\mathrm{i}})} \cdot \frac{(N_{\mathrm{s}}+1)L}{2} \cdot \frac{1}{\cos(\theta_{\mathrm{sg}})} \tag{26}$$

where L is the antenna length, c_0 is the velocity of light, W_{rg} is the pulse bandwidth, and $n_{\mathrm{s}} \in [2, \ldots, N_{\mathrm{s}}]$ the subswath number. Since the resolution is dependent on incident and squint angle, the number of looks varies across the swath as well. Fixing the bandwidth to 10 MHz and the antenna length to 4 m results already in an available number of looks in the order of 200 000 (single swath case). The corresponding 2-D resolution is then in the order of 80 m^2 for a product resolution of 4×4 km^2.

6) Fore and Aft Velocity Vector Combination: Finally, having all variables of (18) available, the surface velocity performance can be evaluated for each polarization separately. The combination of the 2-D velocity vector for each point along ground range is necessary, since all contributions are still in the (on-ground projected) LoS direction, which varies across the swath. Basically, this means a geometric transformation of both vectors $v_{\mathrm{r,p}}^{\mathrm{fore}}$ and $v_{\mathrm{r,p}}^{\mathrm{aft}}$ into a common coordinate system, preferably azimuth and ground range, v_{az} and v_{gr}, which denote the components of the total velocity vector $\vec{v}$.

This article has been accepted for inclusion in a future issue of this journal. Content is final as presented, with the exception of pagination.

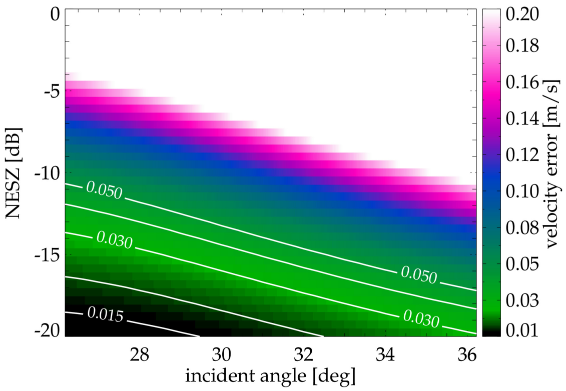

Fig. 8. Interferometric TSCV performance: surface velocity error $\sigma_{v_{\mathrm{r,p}}}$ in m/s. Quantitative result of the flowchart in Fig. 5 for 18.5° squint angle, a product resolution of 4×4 km^2, and 798-km orbit height.

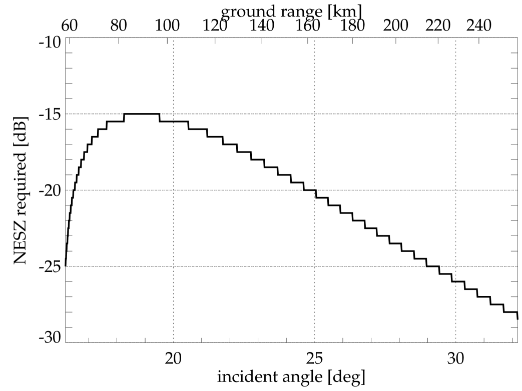

Fig. 9. Illustration of strong variation of the required NESZ for a surface velocity error of 3 cm/s at a 500-km orbit: optimized by applying a 13.5° squint angle.

Under the assumption of neglecting the wind contribution, or rather a GMF considering also the wind (see Section II-B), a straightforward (geometric) transformation can be written as

$$\begin{aligned} v_{\mathrm{r,p}}^{\mathrm{fore}} &= v_{\mathrm{gr}} \cos(\theta_{\mathrm{sg}}) + v_{\mathrm{az}} \sin(\theta_{\mathrm{sg}}) + n^{\mathrm{fore}} \\ v_{\mathrm{r,p}}^{\mathrm{aft}} &= v_{\mathrm{gr}} \cos(\theta_{\mathrm{sg}}) - v_{\mathrm{az}} \sin(\theta_{\mathrm{sg}}) + n^{\mathrm{aft}} \end{aligned} \tag{27}$$

where n denotes the noise or velocity error $\sigma_{v_{\mathrm{r,p}}}$, respectively. The corresponding matrix formulation will be

$$\vec{v}_{\mathrm{r,p}} = \boldsymbol{M}\vec{v} + \vec{n}. \tag{28}$$

Estimating the 2-D velocity $\vec{v}$ with the inverse (without any *a priori* information), the error covariance matrix results in

$$\boldsymbol{R}_{\mathrm{v}} = E\{(\vec{v} - \vec{\mu}_{\mathrm{v}})(\vec{v} - \vec{\mu}_{\mathrm{v}})^T\} = \boldsymbol{M}^{-1}\boldsymbol{R}_{\mathrm{n}}\boldsymbol{M}^{-T} \tag{29}$$

where μ_v is the expected value of v_{az} and v_{gr}, respectively, and $\boldsymbol{R}_{\mathrm{n}}$ is the covariance matrix of the noise in the measurement $\vec{v}_{\mathrm{r,p}}$. The eigenvalues of $\boldsymbol{R}_{\mathrm{v}}$ represent the variance of the transformed velocity along the two orthogonal directions: azimuth and ground range. The trace is the total variance. Therefore, either a worst case error direction can be detected, e.g., if a requirement for a maximum error in any direction is given, or the velocity error can be approximated by projecting the error in the direction of the surface velocity

$$\sigma_v \approx \sqrt{\frac{\vec{v}^T}{\|\vec{v}\|}\boldsymbol{R}_{\mathrm{v}}\frac{\vec{v}}{\|\vec{v}\|}}. \tag{30}$$

This finally concludes the full interferometric performance calculation shown in Fig. 5. The 2-D surface velocity error can be evaluated. Fig. 8 shows the error depending on incident angle and NESZ for some exemplary inputs. In this example, an NESZ in the range of -20 to -11 dB is necessary to achieve the aim of 3–5 cm/s velocity error.

V. Instrument Design and Tradeoffs

The instrument concept design is based on the interferometric performance, since the (random) interferometric measurement error of the surface velocity cannot be eliminated. The objective is the derivation of an SAR instrument requirement, characterized by the NESZ or NESZ-resolution trade-space, respectively, from given mission requirements, primarily the surface velocity accuracy. This can be performed by an iterative or backward calculation of the interferometric performance. In order to fulfill all mission requirements on the most demanding parameters, such as product resolution, swath coverage, and minimum wind speed, several tradeoffs have to be considered. These are discussed in the following.

A. Tradeoffs

1) Wind Speed and Direction: In order to guarantee the performance over all possible wind conditions, a worst case assumption is inevitable. Since the NRCS is low for low wind speeds, the instrument sensitivity has to be high. Therefore, the worst case means the lowest wind speed at which a measurement is required to be valid. Wind speeds of 2–3 m/s are already an ambitious goal. However, this is the scientifically required minimum wind speed U_{10} at which measurements are still expected to be valid.[3] The same accounts for the wind direction, although not that severe as for the wind speed. The weakest signal return is obtained in case the wind direction is orthogonal to the LoS direction. Assuming an optimum squint angle of 45° results in a worst case wind direction of 135° or 315°. The logical consequence of these assumptions is that for most (wind) conditions, the system is overdesigned.

2) Squint Angle: The essential geometric inputs are the incident angle and the squint angle on-ground. Principal geometry issues can be found in the literature [33], except for the setting and tuning of the squint angle in the particular case of electronic beam steering. The squint angle has to be optimized in such a way that the resulting NESZ is as equal as possible in near and far range of the swath. An example is given in Fig. 9. We can observe that naturally the requirement on the instrument sensitivity increases quite linearly toward far range resulting from the dominant impact of the incident angle, but drops almost logarithmically in near range, which is mainly due to the impact of the strongly increasing on-ground squint angle in near range. This fact of course increases with a larger swath width and is not worth mentioning in the case

[3]The index of the wind speed (U_{10}) denotes that it is correlated with a height of 10 m above the water surface.

of a narrow swath. Note that a small change in squint angle yields a strong variation of the required sensitivity in near range. This is also naturally linked to the orbit height with its corresponding incident angle range. In Fig. 9, a low orbit height of approximately 500 km was chosen in order to clearly visualize the problem. For an equalization of the required sensitivity (see Fig. 8), while keeping the swath width, one has to increase the orbit height.

3) Ambiguity Ratio and Coherence: The coherence can be divided into several contributions, which means a large trading space, since a worsening of the requirement for each single contribution can be compensated by raising another one. In principle, setting a value close to 1 means a strong requirement with respect to this parameter. The quantization contribution and temporal contribution ($\gamma_{\mathrm{quant}}, \gamma_{\mathrm{t}}$) are already described in Section IV-C. For γ_{amb}, we use a similar approach. A reasonably high value is set to establish a high requirement for our system in order to ensure no ambiguity problems. The ambiguity ratio and (23) can be used to set γ_{amb} by applying empirical numbers. For example, assuming a DTAR of -14 dB as a worst case scenario yields $\gamma_{\mathrm{amb}} = 0.96$. However, the DTAR, representing the total ambiguity ratio, is only valid for a target area and an ambiguity area having the same backscatter. This seems to be not very likely, at least for range ambiguities. For typical spaceborne SAR missions, the azimuth ambiguity signal is scattered from areas in the order of less than 5 km apart, whereas the range ambiguity signal arrives easily from areas 100 km apart from the target area. Thus, it is beneficial to consider them separately, and distribute the assumed DTAR value between the azimuth-ambiguity-to-signal-ratio (AASR) and range-ambiguity-to-signal-ratio (RASR). In order to account for the large distance, where the range ambiguities coming from, one can assume a more likely NRCS value like the global mean for the ocean. Therefore, we consider the target area with a worst case wind speed of 2 m/s, but we assume for the ambiguity area the mean global wind speed of around 6.5 m/s [61]. Using our NRCS-model, we can derive a backscatter difference to be subtracted additionally from the RASR. Note that this assumption can be still too weak considering coastal areas. Finally, adjusting the γ_{SNR} means a tuning of the (required) instrument NESZ [see (19) and (21)], which is finally the value we are aiming at, until the required product accuracy is reached. These considerations also yield that γ_{amb} should be *at least* $\geq \gamma_{\mathrm{SNR}}$.

4) Number of Looks (Resolution Versus SNR): The number of looks is an important figure for the interferometric performance. Generally, a large number of looks is favorable, since averaging reduces noise in the final product. However, the full context is a little bit more complex. More looks are achieved by a better resolution, which means a larger pulse bandwidth.[4] But more bandwidth results in more thermal noise and therefore more thermal decorrelation. At some point, the thermal noise becomes relevant and will limit the reduction of nonthermal decorrelation by averaging. Therefore exists an optimum, i.e., an upper limit, for the system bandwidth.

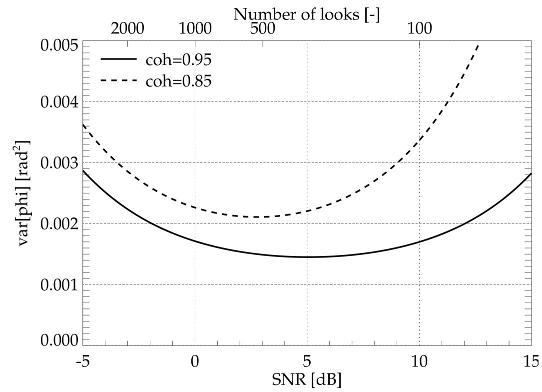

Fig. 10. Variance of the interferometric phase and dependence on SNR and the number of looks.

By investigating the phase variance in Fig. 10, we can take a closer look to this tradeoff. Fig. 10 is generated by applying (18) in dependence of the SNR and the number of looks, where 0-dB SNR was arbitrarily set to 1000 looks. The given coherence comprises only the system and temporal contribution. We can observe that if the coherence is rather high, then the optimum, in terms of final phase variance, is shifted toward a better SNR. The interpretation is that we have to take care that good nonthermal coherences are not deteriorated by a low SNR. On the other hand, if the starting coherence is low, then one should prefer a slightly worse SNR in order to gain number of looks for averaging. For example, in the case of a small temporal baseline, the temporal coherence will be rather high and therefore, the optimum SNR is around 5 dB. But for acceptable coherence values, the optimum is still around 0–5 dB and since the optimum is broad, variations of the SNR of 5 dB have almost no consequences for the final performance. Therefore, this tradeoff does not seem to be too critical. However, the SNR has to be monitored during the design process and performance calculations.

5) Instrument Requirement Space (NESZ Versus 2-D Resolution): After considering all tradeoffs in the (iterative) performance calculation, we finally end up with an NESZ, which fulfills the given science requirements. We call this instrument (or NESZ) requirement and it represents the input for the design of the instrument concept. Since the geometric resolution is not a predetermined figure and the detailed relation of azimuth and range resolution is not relevant in this context, we evaluate an NESZ requirement for a large range of feasible 2-D resolutions (ρ_{2D}) in order to obtain a quantity of possible solutions. Fig. 11 shows an example of such an instrument requirement space. For example, we can extract for 30° incident angle and for a 2-D resolution of 600 m^2, a necessary NESZ of around 20 dB in order to obtain the assumed surface velocity accuracy of 3 cm/s. Generally, one can observe that following a line of constant NESZ toward far range requires a more demanding (better) resolution.

[4]The pulse bandwidth corresponds to the range direction. The azimuth resolution variation does not affect the thermal noise, and can be increased in order to increase the number of looks. However, in a typical imaging scenario, range resolution and azimuth resolution are intended to deviate not too much from each other, since both being in the same order of magnitude ensures a constant image quality.

This article has been accepted for inclusion in a future issue of this journal. Content is final as presented, with the exception of pagination.

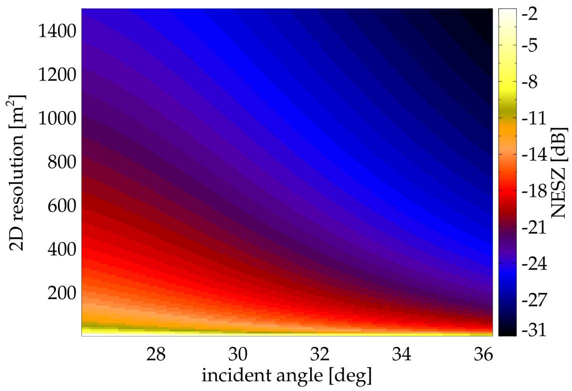

Fig. 11. Instrument requirement (space): required NESZ versus 2-D resolution. It shows the NESZ (in dB), which is required to fulfill a surface velocity accuracy of 3 cm/s.

This constitutes the main trading space for the instrument concept design and we have finally concluded the whole chain from the science requirements to the instrument requirements.

B. Instrument Concept Derivation

The instrument concept can be designed based on the derived instrument requirement space. The tradeoff takes place between the NESZ and both 1-D resolutions, azimuth and range, whose product yields the 2-D resolution. Both can be almost arbitrarily traded because for each NESZ value, the number of looks is chosen such that the required product resolution is achieved. The usage of the ScanSAR imaging mode offers now an advantage to the concept design. Since the geometric resolution does not necessarily has to be equal across the swath coverage (neither 1-D nor 2-D), the instrument requirement space offers the opportunity of setting a better (geometric) resolution in a far range (sub)swath in order to compensate the increasing demand of sensitivity in far range. This means the design will consist of several subswaths with different pulse bandwidths and/or different processed azimuth bandwidths, such that the 2-D resolution becomes better per each subswath toward far range. In other words, the resolution is improved where it is needed, which ensures that the required NESZ stays at a more or less constant level. Obviously, the higher the number of subswaths, the more accurate we can follow a certain NESZ level. But increasing the number of subswaths means, on the other hand, also a decrease of the azimuth resolution [see (26)]. However, this additional degree of freedom helps in order to solve the design task, where mission requirements dictate strong limits.

VI. Systematic Errors

After dealing with the measurement noise by interferometric performance evaluation, we also have to determine and calibrate for the systematic errors in order to eliminate their impact. But in fact, the calibration of ATI measurements over open ocean is difficult. Phase calibration is typically achieved using land included in the observed scene as a reference. This implies that the system must rely on this "standard" method, on internal calibration and on very slow drifting systematic

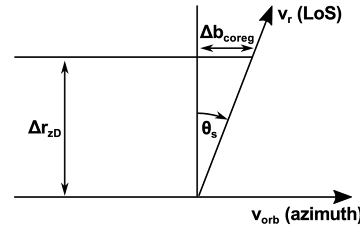

Fig. 12. Illustration of coregistration error Δb_{coreg} (in the slant range plane) resulting from a slant range error.

errors during the acquisitions over the ocean. In the following, the systematic errors of a dual-beam system are identified and discussed. The squint angle, which is a crucial figure in this analysis, is always assumed to be 18.5° in accordance to our instrument concept.

A. Attitude or Pointing (Knowledge) Error

A pointing error has an impact on the ATI phase and hence on the surface velocity error. With regard to a yaw, pitch, or roll steering error ($\xi_{\text{yaw}}, \xi_{\text{pitch}}$, and ξ_{roll}), we can derive a deviation in the (zero-Doppler) slant range distance (Δr_{zD}), since this deviation has an impact on the velocity error. Considering (3), the (radial) surface velocity error can be expressed as

$$\Delta v_{\text{r}} = \frac{\Delta r_{\text{zD}}(\xi)}{2\cos(\theta_{\text{s}})\tau_{\text{ATI}}}. \tag{31}$$

In order to simplify the calculation of the slant range error, basically the misaligned baseline vector (by ξ) is transformed into the slant range plane of the system. We start with an attitude error matrix $\boldsymbol{A}_\xi = \boldsymbol{R}_{\text{z}}(\xi_{\text{yaw}})\boldsymbol{R}_{\text{y}}(\xi_{\text{roll}})\boldsymbol{R}_{\text{x}}(\xi_{\text{pitch}})$, where $\boldsymbol{R}$ denotes a Cartesian rotation matrix, and a baseline vector $\vec{b}$, which is then projected by $\boldsymbol{P}$ into the slant range plane, yielding the slant range error vector

$$\Delta\vec{r}_\xi = \boldsymbol{P}\boldsymbol{A}_\xi\vec{b} \tag{32}$$

where $\boldsymbol{P} = \boldsymbol{R}_{\text{y}}(\theta_{\text{l,zD}}(r))$ and $\theta_{\text{l,zD}}(r)$ indicates the look angle in zero Doppler direction with $\cos(\theta_{\text{l,zD}}(r)) = \cos(\theta_{\text{l}}(r))/\cos(\theta_{\text{s}})$. Finally, the z-component of $\Delta\vec{r}_\xi$ represents the slant range distance error Δr_{zD} responsible for the surface velocity error.

Additionally, every slant range error yields a *coregistration error* in a squinted geometry case. Fig. 12 shows this fact. If the slant range distance is assumed wrongly in the azimuth coregistration process, the resulting ATI baseline error is

$$\Delta b_{\text{coreg}} = \Delta r_{\text{zD}}\tan(\theta_{\text{s}}) \tag{33}$$

assuming a symmetric squint angle in the fore- and aft-looking direction. Now the surface velocity error follows from:

$$\Delta v_{\text{r}} = \frac{\Delta b_{\text{coreg}}\sin(\theta_{\text{s}})}{\tau_{\text{ATI}}} \tag{34}$$

using $\Delta\phi_{\text{ATI}} = 2\pi f_{\text{Dc,sys}} \cdot \Delta b_{\text{coreg}}/v_{\text{orb}}$ with (11).

The (fore and aft) radial attitude errors and their corresponding coregistration errors can be summed up and transformed straightforward into azimuth (Δv_{az}) and ground range (Δv_{gr}) velocity errors. Δv_{gr} is presented in Fig. 13(a) for a 1-μrad

This article has been accepted for inclusion in a future issue of this journal. Content is final as presented, with the exception of pagination.

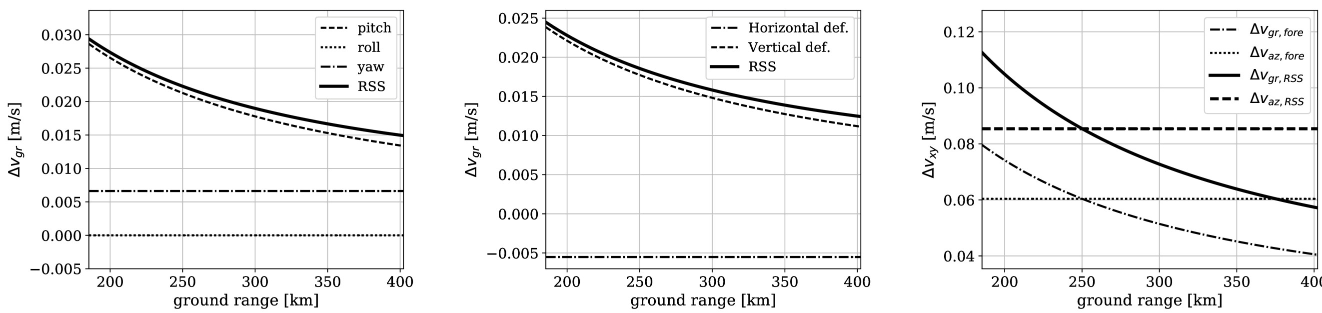

(a) Velocity error w.r.t. attitude (b) Velocity error w.r.t. deformation (c) Velocity error w.r.t. phase

Fig. 13. Impact of systematic errors on surface velocity. Surface velocity error due to (a) attitude error of 1 μrad in yaw, pitch, and roll (only Δv_{gr} component, since $\Delta v_{\mathrm{az}} = 0$) and RSS error, (b) vertical and horizontal deformation error of 10 μm (only Δv_{gr} component, since $\Delta v_{\mathrm{az}} = 0$) and RSS error, and (c) instrument phase error of 1° with respect to fore-looking direction (aft-looking error accordingly), RSS error includes both directions.

rotation error around each axis. We observe that the pointing error does not have any impact on azimuth ($\Delta v_{\mathrm{az}} = 0$), since it cancels out with respect to both look directions. Note that the pitch error with up to 2.8 cm/s is the largest contribution (of yaw, pitch, and roll) to the root-sum-squared (RSS) error and the roll error is zero. All coregistration errors are significantly less than the attitude error itself (not shown). Furthermore, it can be verified that the velocity error derived from all attitude effects is exactly identical to the one derived from the DCA.

B. Two-Dimensional Deformation Error

The deformations can occur as longitudinal or transversal changes in the relative phase center positions. In the longitudinal case, i.e., stretching or compression, they should be negligible. Only the coregistration error contribution due to the squint angle has a small effect. However, we consider in the following only relative transversal deformations. Deformation errors are similar to attitude errors, since a structural deformation results most probably in an antenna mispointing. In this analysis, we assume that the deformations have a quadratic shape, which can be divided into two cases. Even deformations yield an identical displacement of the two phase centers and therefore no ATI measurement error. Since the beam patterns are expected to be slightly tilted, a Doppler centroid measurement will exhibit a deviation for each phase center. Odd deformations will cause an ATI error, which is expected to be identical to the Doppler centroid error (due to an assumed identical tilt of the beam patterns) and therefore cannot be distinguished from a pointing error.

In order to analyze the transversal deformation errors, we start with a baseline and add a vertical or horizontal error. This baseline is then projected into the slant range plane with operator $\boldsymbol{P}$ used in (32). Then, we obtain again the radial or rather the azimuth and ground range surface velocity errors in the same manner like in the attitude error case [see (31)]. The coregistration error (34) has to be considered as well. Fig. 13(b) shows a maximum ground range velocity error around 2.5 cm/s for a relative vertical and horizontal deformation of 10 μm and the corresponding RSS error. The azimuth error cancels out again due to symmetry reasons. The vertical deformation corresponds in principle to a pitch attitude error and induces therefore a larger error than the horizontal deformation.

C. Instrument Phase Error

The sensitivity of the instrument or receiver phase can be directly evaluated by solving (3) for v_{r} and transformed into azimuth and ground range direction. Fig. 13(c) shows the effect of a 1° relative phase error on the surface velocity error between the two fore beams. The error behavior in the aft direction is identical with respect to ground range, but has the opposite sign with respect to azimuth, due to different signs of the fore- and aft-Doppler measurement. The RSS error includes both directions appropriately.

D. Orbit (Knowledge) Error

For the sake of completeness, the platform motion error shall be mentioned although it is supposed to be small (see Table III). Since motion is relative, a platform motion error is not distinguishable from the surface velocity. An along-track orbit velocity error translates directly into an along-track surface velocity error $\Delta v_{\mathrm{az}} = \Delta v_{\mathrm{orb,az}}$. The cross-track error is given by a potential cross-track error component of the orbital velocity $\Delta v_{\mathrm{gr}} = \Delta v_{\mathrm{orb,zD}} / \sin(\theta_{\mathrm{i,zD}})$. The incident angle scaling at the zero Doppler position takes into account that we measure errors projected in the slant range plane.

VII. Instrument Concept

This section presents a mission and instrument concept, which was developed according to the methodology in this paper. The concept was developed in the framework of the ESA *Ocean Surface Current Mission Study (OSCMS)* [62], [63] and slightly adapted in this analysis. The driving mission requirements in Table I were given and represent the state-of-the-art scientific needs. These were used to derive the instrument requirements. The resulting requirement space is the one presented in Fig. 11.

A. OSCM Instrument

The basic concept is a javelin system structure, shown in Fig. 14, with electronically steered phased-array antennas in order to benefit from smaller receive echo windows. The single

TABLE I
DRIVING MISSION REQUIREMENTS FROM ESA

Revisit time	2-10 days
Spatial coverage	Global
Repeat coverage	<20 days
Swath coverage	≥ 200 km
Surface velocity accuracy	5 cm/s
Wind velocity accuracy	2 m/s
Minimum surface wind (U_{10})	3 m/s
Product resolution	1-4 km
Operating frequency	Ku-band

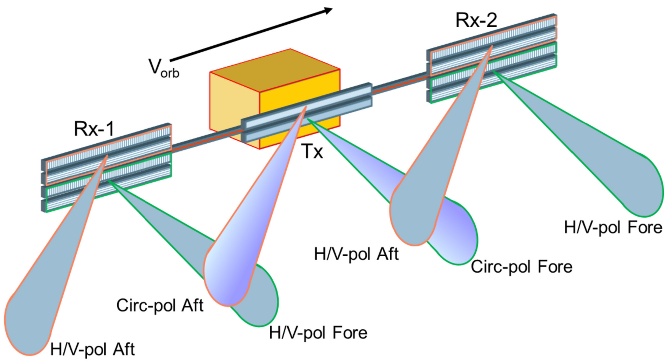

Fig. 14. Canonical instrument concept and antenna configuration. Tx antenna setup in the center with circular polarization: fore- and aft-looking, (total height 0.84 m). Two Rx antenna setups with orthogonal linear polarization, each consisting of four subantennas: fore- and aft-looking, two polarizations in interleaved structure (total height 1.6 m).

TABLE II
MAIN INSTRUMENT AND OPERATING MODE PARAMETERS. TOTAL ANTENNA HEIGHT FOR TX CASE: 4 m × 0.21 m, FOR EACH RX CASE: 2 m × 0.8 m DUE TO INTERLEAVED H/V CONCEPT

Acquisition Geometry			
Orbit height	798 km	ATI baseline	12 m
Azimuth squint	$\pm 18.5°$	Antenna tilt	$20.1°$
Antenna			
Single Transmit Sub-Antenna		Single Receive Sub-Antenna	
Length	3.6 m		3.6 m
Height	0.21 m		0.8 m
Number of rows	12		44
Gain	41.34 dB		47.23 dB
Losses	2.35 dB		2.68 dB
Polarization	Circular*	2 lin. orthog. channels	
Avg. Tx RF power	320 W	Noise temp.	400 K
Operating Mode			
SAR mode	ScanSAR	DBF mode	SCORE
Number of bursts	3	Swath coverage	202 km
Pulse duty cycle	12%	Data rate	598.4 Mbit/s
Pulse bandwidth	10/10/10 MHz		
PRF	3780/3830/3880 kHz		
Proc. Doppler bandwidth	168/346/840 Hz		

*) The single Tx sub-antenna is linearly polarized but orthogonal and 90° phase-shifted to its adjacent one, which yields the circular pol.

side-looking system provides the required 200 -km coverage in a continuous swath with respect to elevation. Note that global coverage in one repeat cycle is already achieved by a swath width of around 150 km. The 12 -m physical baseline between both Rx phase centers corresponds to around 550λ, which is within the desired accuracy (see Fig. 1) for an optimum SNR range of around 0–10 dB (see Fig. 10). The main instrument parameters of the concept are summarized in Table II.

In order to achieve the large coverage and the high sensitivity, a ScanSAR imaging mode with three subswaths is applied, which exhibit cross-track widths of 84, 62, and 56 km, respectively. However, due to the demanding NESZ requirement, the introduction of digital beamforming (DBF) techniques is indispensable in order to achieve the performance using available levels of RF power. Therefore, SCan-On-REceive (SCORE) [64], [65] is introduced within each of the subswaths. In order to reduce the number of digital channels for the onboard real-time beamforming, four elements/rows can be combined from a performance point of view, yielding 11 channels for each subantenna. This combination has been optimized with respect to the required sensitivity and means an NESZ decrease of $\leq$1 dB. The better sensitivity due to SCORE has to be paid by an increase of each Rx subantenna height, in this case by a factor of around 4 compared with the Tx antennas. It yields a height of 0.8 m for each single Rx subantenna.

Given that two sets of four Rx subantennas are necessary to form the along-track interferometer, and in order to minimize losses, a *canonical* antenna system is proposed (see Fig. 14). The narrow (in elevation) Tx antennas are center mounted, while the wider Rx antennas are mounted at both ends of a deployable structure that provides the required ATI baseline. In the transmit case (of the narrow antenna), each of the fore- and aft-looking one consists of a circular polarized antenna. Each circular polarization is generated in turn by two linearly polarized and physically separated subantennas with a 90° phase shift and a height of 0.21 m. Therefore, the total Tx antenna height is 0.84 m. In both Rx cases, each of the fore and aft squinted antennas comprises two linearly polarized subantennas with an interleaved structure in order to form the hybrid polarization and simultaneously not double the antenna height. Due to his interleaving of the horizontal and vertical polarized waveguides, the overall Rx antenna height of 1.6 m is approximately only twice as large as in the Tx case. The antenna length in azimuth of 3.6 m is a result of the resolution and ambiguity requirements taking into account the large azimuth squint angle. The required average RF power of each Tx subantenna is 320 W, which results in a total average RF power consumption of 1280 W.

B. OSCM Performance

The parameters incident angle, squint angle, and orbit height were determined by carrying out a sensitivity-based optimization. The incident angle range of 26.2°–36.2° [see Fig. 15(a)] is chosen to be as far as possible in the far range in order to improve the wind and velocity retrieval process and to decrease the impact of systematic errors (see Section III-B). A relatively high orbit (with respect to a Vega-class launcher) of 798 km reduces the impact of the swath width on the spreading of the incident angle range. The electronic azimuth antenna steering results in a range-dependent variation of the ground-projected squint angle from 37.3° to 54.1° [see Fig. 15(b)] for a squint angle of 18.5°. This angle is optimized

This article has been accepted for inclusion in a future issue of this journal. Content is final as presented, with the exception of pagination.

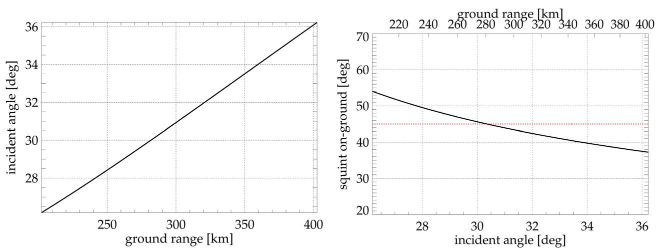

(a) (b)

Fig. 15. Variation of (a) incident angle in LoS and (b) squint angle on-ground (horizontal line illustrates the ideal, constant case of 45°). Both figures show the full 200-km coverage.

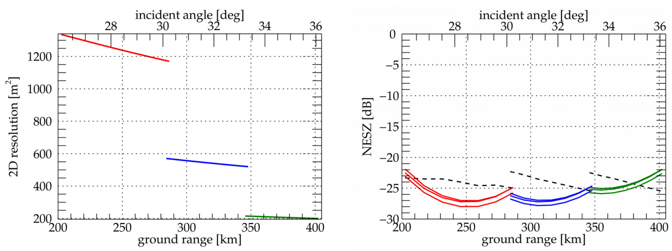

(a) (b)

Fig. 16. (a) Two-dimensional single-look resolution for the proposed design. (b) Achieved NESZ at three different azimuth positions due to scalloping (solid lines), and the NESZ requirement (dashed lines).

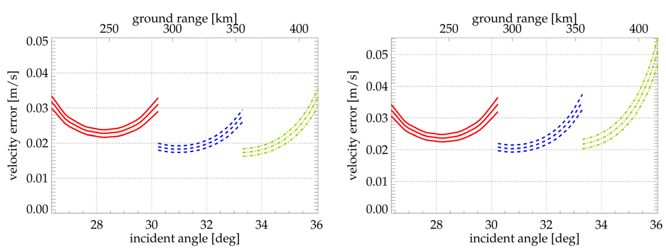

(a) (b)

Fig. 17. Interferometric error of the surface velocity. (a) VV. (b) HH.

with respect to its optimal 45° on-ground projection and a preferably uniform NESZ.

The *SAR performance* achieved by the system is shown for the single-look 2-D resolution in Fig. 16(a) and for the NESZ in Fig. 16(b). The 1-D resolutions are according to the bandwidths given in Table II around 30 m in range and 29, 16, and 7 m in azimuth for each subswath. The burst length and the pulse bandwidth have been optimized for all three ScanSAR subswaths. By applying better resolution for increasing incident angles, the NESZ is equalized across the full coverage. The NESZ shows for each subswath three relative azimuth positions, revealing the scalloping associated with ScanSAR imaging. The dashed lines show the NESZ requirement for the resolution provided, in order to obtain the required surface velocity performance. The requirement is not fully met for the last 10 km in far range. The range and azimuth ambiguity ratios are below −24 and −17 dB, respectively.

The *interferometric performance* is presented in Fig. 17. According to the NESZ, one can observe the three subswaths

TABLE III

SYSTEMATIC ERRORS (THE DEFORMATION ERROR IS INCLUDED WITHIN THE ATTITUDE ERROR AND ONLY LISTED FOR COMPLETENESS)

Parameter	Assumed accuracy	Velocity error ground range	Velocity error azimuth
Attitude	0.75 μrad	0.012-0.023 m/s	–
(Deformation)	(10 μm)	(0.013-0.025 m/s)	(–)
Instrument phase	0.17°	0.010-0.019 m/s	0.014 m/s
Orbit	3 mm/s	0.0006-0.0012 m/s	0.0003 m/s
RSS error	–	0.015-0.03 m/s	0.014 m/s

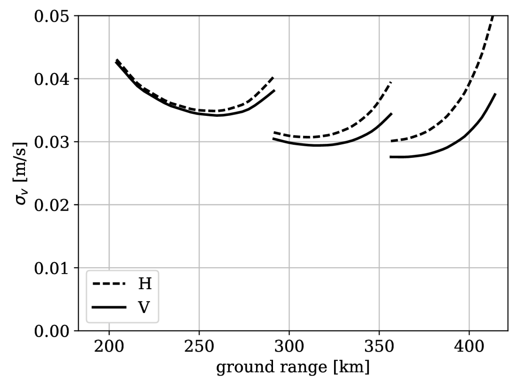

Fig. 18. Final surface velocity system (RSS) error (including systematic errors) for VV polarization and HH polarization.

as well as the ScanSAR-related scalloping. Except for the last few kilometers of ground range, the interferometric error is almost within its budgeted requirement of 3 cm/s and leaves approximately 2 cm/s for the systematic errors. These are given for attitude, deformation, instrument phase drift, and platform motion in Table III, and are estimated based on state-of-the-art technology. Combining both error sources by calculating the overall RSS error, we end up with a final *system-based* surface velocity error in Fig. 18. The requirement of 5-cm/s absolute surface velocity accuracy is achieved, and we can clearly observe that the high sensitivity requirement in far range is a driving and demanding parameter. Note that the 5-cm/s absolute velocity error does not account for inversion errors, like described in detail in Sections II-B and III-C. It is purely related to the system and the measured Doppler velocity. Even with this approach, the requirement of 5 cm/s is very challenging, since it results in a large instrument.

VIII. CONCLUSION

We have presented a methodology to design a spaceborne SAR system based on dual-beam ATI in order to measure 2-D ocean surface velocities. We have extensively discussed all fundamental issues, such as the measurement concept, the geophysical principles, the observation geometry and antenna concept, the optimal interferometric baseline, the different error contributions, the system frequency, and the advantage of polarization diversity. Based on a simple, sensitivity-based performance model, the main focus is on the derivation of an instrument requirement space, namely, the NESZ versus 2-D resolution tradeoff, from scientific requirements, such as, for example, the surface velocity accuracy. The evaluation of the underlying interferometric performance is shown, including the performance model, the RCS model, polarization mixing in the case of electronically squinted antenna beams, all coherence contributions, the SNR determination, the resolution and number of looks dependence, and finally, the 2-D combination of both squinted LoS surface velocity vectors. Based on the resulting NESZ requirement, the instrument design with all necessary tradeoffs in terms of NESZ, pulse bandwidth/SNR, ambiguities, and minimum wind speed is explained. The methodology is finally applied to the OSCM study of ESA, a carefully traded, single platform system concept in Ku-band, which fulfills the mission requirements, such as a surface velocity accuracy of 5 cm/s, 200-km swath coverage, and a product resolution of $4 \times 4\,\mathrm{km}^2$.

Altogether, the presented methodology is feasible to design a spaceborne SAR system, which supports the extraction of 2-D ocean surface velocities. The OSCM concept illustrates the importance of the aforementioned design parameter tradeoffs. It furthermore reveals that the huge sensitivity requirement due to the desired accuracy, results in large demands for instrument power, size, and mass. Therefore, we would like to point out the main available and dominant parameters having a major impact on the design, which are: 1) the product resolution; 2) the swath coverage, since far range is always more demanding in terms of power; and 3) the wind dependence, which means the minimum considered wind speed, for which the measurement is valid. Note that a "small" relaxation of all three mentioned parameters—for example, 1 m/s in wind speed—can already yield a halving of the instrument requirements and therefore also the size. Hence, one has to carefully consider how accurate the measurements have to be regarding spatial resolution and temporal resolution. In other words, a submesoscale specification is highly demanding.

Clearly, we have to state again that ocean surface velocity retrieval is always coupled with wind retrieval and involves an inversion process to obtain the desired velocity or current components from the measured Doppler velocity. In our system-based approach, we do not consider any geophysical inversion. Nevertheless, we propose to apply polarization diversity in order to support the inversion process. A consistent model, considering all involved parameters, would allow a quantification (instead of a qualitatively tradeoff) of important system parameters like the optimal incident angle range, since it depends not only on sensitivity, but also on the scatterometry, polarization diversity, and the systematic errors. Furthermore, the coupled wind and velocity accuracy have an impact on each other. Hence, a coarse wind measurement accuracy spoils any good surface velocity measurement and vice versa. This has to be taken into account when setting up requirements for any ocean SAR mission regarding wind and velocity observations. However, data from spaceborne dual-beam ATI SAR observations of the ocean surface will doubtlessly provide valuable information about ocean surface velocities and the presented methodology and tradeoffs are well suitable to derive an instrument concept for such a mission.

APPENDIX A
GEOMETRIC DERIVATION OF POLARIZATION FACTORS

The basic operation in order to derive the polarization factors is a simple projection of the total electric field vector onto the horizontal and vertical polarization directions of the Earth surface. It follows a description approach of the relation between the *linear* antenna polarizations and the H and V on-ground polarizations.

A linearly polarized electric field is fully described by two (scalar) components $|\vec{E}_\theta^{m,A}(\vec{r})|$ and $|\vec{E}_\phi^{m,A}(\vec{r})|$ in a spherical coordinate system, where A denotes the antenna coordinate system, $\vec{r}$ denotes the position vector, and $m \in \{1,2\}$ the channel.[5] From this (typical) starting point, we introduce the vectorial character by using the unit vectors $\vec{u}_\theta$ and $\vec{u}_\phi$

$$\begin{aligned}\vec{E}_\theta^{m,\mathrm{A}}(\vec{r}) &= |\vec{E}_\theta^{m,\mathrm{A}}(\vec{r})|\,\vec{u}_\theta(\vec{r})\\ \vec{E}_\phi^{m,\mathrm{A}}(\vec{r}) &= |\vec{E}_\phi^{m,\mathrm{A}}(\vec{r})|\,\vec{u}_\phi(\vec{r})\end{aligned} \tag{35}$$

where $|E_\theta|^2 + |E_\phi|^2 = 1$. The unit vectors are now expressed in terms of Cartesian coordinates in order to introduce a linear polarization representation

$$\begin{aligned}\vec{u}_\theta(\vec{r}) &= \vec{u}_\mathrm{x}\cos(\theta_\mathrm{a})\cos(\phi_\mathrm{a}) + \vec{u}_\mathrm{y}\cos(\theta_\mathrm{a})\sin(\phi_\mathrm{a}) + \vec{u}_\mathrm{z}\sin(\theta_\mathrm{a})\\ \vec{u}_\phi(\vec{r}) &= -\vec{u}_\mathrm{x}\sin(\phi_\mathrm{a}) + \vec{u}_\mathrm{y}\cos(\phi_\mathrm{a})\end{aligned} \tag{36}$$

where θ_a and ϕ_a denote the antenna steering direction and x, y, and z are aligned with the antenna. Note that the unit vectors in the spherical coordinate system are a set of vectors each, since they depend on their position $\vec{r}$, or $\{\theta_\mathrm{a}, \phi_\mathrm{a}\}$, which is varying across the swath. Now, after forming the total field vector, one can apply the transformation from the antenna coordinate system into the Earth-centered system (E)

$$\vec{E}^{m,\mathrm{E}}(\vec{r}\,') = \boldsymbol{Q}\cdot(\vec{E}_\theta^{m,\mathrm{A}}(\vec{r}) + \vec{E}_\phi^{m,\mathrm{A}}(\vec{r})) \tag{37}$$

where the operator $\boldsymbol{Q}$ describes the rotation with respect to the antenna attitude as well as the antenna steering depending on the individually applied coordinate systems. The dashed position vector corresponds to the changed coordinate system.

Finally, we can apply the projection of the vector to the H and V polarization on-ground by using the scalar product with the H and V unit vectors related to the ground

$$\begin{aligned}E_\mathrm{H}^{m,\mathrm{E}}(\vec{r}\,') &= \vec{E}^{m,\mathrm{E}}(\vec{r}\,')^T\,\vec{u}_\mathrm{H}(\vec{r}\,')\\ E_\mathrm{V}^{m,\mathrm{E}}(\vec{r}\,') &= \vec{E}^{m,\mathrm{E}}(\vec{r}\,')^T\,\vec{u}_\mathrm{V}(\vec{r}\,').\end{aligned} \tag{38}$$

The H polarization is orthogonal to the surface normal $\vec{n}$ and the LoS $\vec{p}$. The V polarization is orthogonal to the H polarization and the LoS. Therefore

$$\vec{u}_\mathrm{H} = \frac{\vec{p}\times\vec{n}}{\|\vec{p}\times\vec{n}\|} \tag{39}$$

$$\vec{u}_\mathrm{V} = \frac{\vec{p}\times\vec{u}_\mathrm{H}}{\|\vec{p}\times\vec{u}_\mathrm{H}\|} \tag{40}$$

where operator $\times$ denotes the cross product. $E_\mathrm{H}^{m,\mathrm{E}}$ and $E_\mathrm{V}^{m,\mathrm{E}}$ with $m \in \{1,2\}$ represent the four polarization factors $\{a_1, a_2, b_1, b_2\}$. Note that the values are dependent on the antenna pattern position on-ground $\vec{r}\,'$.

[5]We only consider the far-field case; therefore, the radial component $\vec{E}_\mathrm{r}$ can be neglected.

APPENDIX B
POLARIZATION RECONSTRUCTION

Assuming a polarization mixing like in the case of an electronically squinted antenna, we have to ensure the correct determination of the polarization scattering coefficients. We consider a linear polarization on receive and a circular polarization on transmit, which is generated by two 90° phase-shifted, orthogonally linear-polarized antennas. These are referred to as channels 1 and 2. The hypothesis for the reconstruction of the scattering coefficients is a low level of cross-polarized backscattering [44].

Starting with the transmitted electric fields E^{t} of channels 1 and 2, we can describe the H- and V-polarized incident electric fields on-ground

$$\begin{pmatrix} E_{\mathrm{H}}^{\mathrm{i}} \\ E_{\mathrm{V}}^{\mathrm{i}} \end{pmatrix} = \begin{bmatrix} a_1 & a_2 \\ b_1 & b_2 \end{bmatrix} \begin{pmatrix} E^{1,\mathrm{t}} \\ E^{2,\mathrm{t}} \end{pmatrix} = \boldsymbol{U} \begin{pmatrix} E^{1,\mathrm{t}} \\ E^{2,\mathrm{t}} \end{pmatrix} \tag{41}$$

by using the polarization factors a and b of Appendix A, where $|a_1|^2 + |b_1|^2 = |a_2|^2 + |b_2|^2 = 1$. The backscattered fields

$$\begin{pmatrix} E_{\mathrm{H}}^{\mathrm{b}} \\ E_{\mathrm{V}}^{\mathrm{b}} \end{pmatrix} = \begin{bmatrix} S_{\mathrm{HH}} & 0 \\ 0 & S_{\mathrm{VV}} \end{bmatrix} \begin{pmatrix} E_{\mathrm{H}}^{\mathrm{i}} \\ E_{\mathrm{V}}^{\mathrm{i}} \end{pmatrix} = \boldsymbol{S} \begin{pmatrix} E_{\mathrm{H}}^{\mathrm{i}} \\ E_{\mathrm{V}}^{\mathrm{i}} \end{pmatrix} \tag{42}$$

result by applying the scattering matrix $\boldsymbol{S}$ under the assumption of a zero cross-polar return. For the received fields of channels 1 and 2, we have to apply the inverse matrix of the polarization factors

$$\begin{pmatrix} E^{1,\mathrm{r}} \\ E^{2,\mathrm{r}} \end{pmatrix} = \boldsymbol{U}^{-1} \begin{pmatrix} E_{\mathrm{H}}^{\mathrm{b}} \\ E_{\mathrm{V}}^{\mathrm{b}} \end{pmatrix} + \begin{pmatrix} n_1 \\ n_2 \end{pmatrix} \tag{43}$$

$$= \boldsymbol{U}^{-1}\boldsymbol{S}\boldsymbol{U} \begin{pmatrix} E^{1,\mathrm{t}} \\ E^{2,\mathrm{t}} \end{pmatrix} + \begin{pmatrix} n_1 \\ n_2 \end{pmatrix}. \tag{44}$$

A noise term n for each channel is added in order to show the effect of noise redistribution. The noise levels correspond to the NESZ of the two channels, which are presumably, but not necessarily, equal. This means $E\{|n_1|^2\} = E\{|n_2|^2\}$, where the NESZ is denoted by the expected value of the noise.

By applying again the transformation to the received fields, we get the desired HH and VV contributions apart from the polarization factors a and b

$$\boldsymbol{U} \begin{pmatrix} E^{1,\mathrm{r}} \\ E^{2,\mathrm{r}} \end{pmatrix} = \begin{pmatrix} E_{\mathrm{H}}^{\mathrm{b}} \\ E_{\mathrm{V}}^{\mathrm{b}} \end{pmatrix} + \boldsymbol{U} \begin{pmatrix} n_1 \\ n_2 \end{pmatrix} \tag{45}$$

$$= \begin{bmatrix} S_{\mathrm{HH}} & 0 \\ 0 & S_{\mathrm{VV}} \end{bmatrix} \begin{bmatrix} a_1 & a_2 \\ b_1 & b_2 \end{bmatrix} \begin{pmatrix} 1 \\ j \end{pmatrix} + \boldsymbol{U} \begin{pmatrix} n_1 \\ n_2 \end{pmatrix} \tag{46}$$

$$= \begin{pmatrix} (a_1 + ja_2)S_{\mathrm{HH}} \\ (b_1 + jb_2)S_{\mathrm{VV}} \end{pmatrix} + \boldsymbol{U} \begin{pmatrix} n_1 \\ n_2 \end{pmatrix} \tag{47}$$

where $E^{1,\mathrm{t}} = 1$ and $E^{2,\mathrm{t}} = j$ in order to account for the circular polarization. Therefore, the scattering coefficients S_{HH} and S_{VV} can be calculated, if NESZ and polarization factors are known.

APPENDIX C
NESZ REDISTRIBUTION

In the derivation of the instrument requirements, we need to know the NESZ of the reconstructed polarizations on-ground. This is solved by a noise redistribution corresponding to (45)

$$n_{\mathrm{HH}} = \frac{n_1 a_1 + n_2 a_2}{a_1 + ja_2} \tag{48}$$

$$n_{\mathrm{VV}} = \frac{n_1 b_1 + n_2 b_2}{b_1 + jb_2} \tag{49}$$

where the noise for each polarization can be evaluated by the noise of channels 1 and 2 together with the polarization factors of Appendix A. Now, the NESZ redistribution is predictable by using again the expected values

$$E\{|n_{\mathrm{HH}}|^2\} = \frac{E\{|n_1|^2\}|a_1|^2 + E\{|n_2|^2\}|a_2|^2}{|a_1 + ja_2|^2} \tag{50}$$

$$E\{|n_{\mathrm{VV}}|^2\} = \frac{E\{|n_1|^2\}|b_1|^2 + E\{|n_2|^2\}|b_2|^2}{|b_1 + jb_2|^2} \tag{51}$$

assuming ideal patterns $|a_1 + ja_2|^2 = |a_1|^2 + |a_2|^2$. The redistributed NESZ is therefore simply a weighting of the noise in the original channels by the polarization factors.

ACKNOWLEDGMENT

The authors would like to thank OHB System AG, responsible for the satellite system and platform design, Macdonald, Dettwiler and Associates Ltd., (MDA), responsible for the technological antenna and instrument design, and the Nansen Environmental and Remote Sensing Center (NERSC), providing scientific support, for the successful joint collaboration in the ESA OSCM study.

REFERENCES

[1] A. Freeman *et al.*, "Ocean measurements from space in 2025," *Oceanography*, vol. 23, no. 4, pp. 144–161, Dec. 2010.
[2] K. Dohan and N. Maximenko, "Monitoring ocean currents with satellite sensors," *Oceanography*, vol. 23, no. 4, pp. 94–103, Dec. 2010.
[3] B. D. Pollard *et al.*, "The wide swath ocean altimeter: Radar interferometry for global ocean mapping with centimetric accuracy," in *Proc. IEEE Aerosp. Conf.*, vol. 2. Sep. 2002, pp. 2-1007–2-1020.
[4] G. B. Bush, E. B. Dobson, R. Matyskiela, C. C. Kilgus, and E. J. Walsh, "An analysis of a satellite multibeam altimeter," *Marine Geodesy*, vol. 8, nos. 1–4, pp. 345–384, Jan. 1984.
[5] R. Fjortoft *et al.*, "KaRIn on SWOT: Characteristics of near-nadir ka-band interferometric SAR imagery," *IEEE Trans. Geosci. Remote Sens.*, vol. 52, no. 4, pp. 2172–2185, Apr. 2014.
[6] R. M. Goldstein and H. A. Zebker, "Interferometric radar measurement of ocean surface currents," *Nature*, vol. 328, no. 6132, pp. 707–709, Aug. 1987.
[7] R. M. Goldstein, H. A. Zebker, and T. P. Barnett, "Remote sensing of ocean currents," *Science*, vol. 246, no. 4935, pp. 1282–1285, Aug. 1989.
[8] H. C. Graber, D. R. Thompson, and R. E. Carande, "Ocean surface features and currents measured with synthetic aperture radar interferometry and HF radar," *J. Geophys. Res. Oceans*, vol. 101, no. C11, pp. 25813–25832, Nov. 1996.
[9] D.-J. Kim, W. M. Moon, D. Moller, and D. A. Imel, "Measurements of ocean surface waves and currents using L- and C-band along-track interferometric SAR," *IEEE Trans. Geosci. Remote Sens.*, vol. 41, no. 12, pp. 2821–2832, Dec. 2003.
[10] R. Siegmund, M. Bao, S. Lehner, and R. Mayerle, "First demonstration of surface currents imaged by hybrid along- and cross-track interferometric SAR," *IEEE Trans. Geosci. Remote Sens.*, vol. 42, no. 3, pp. 511–519, Mar. 2004.
[11] R. Romeiser *et al.*, "Current measurements by SAR along-track interferometry from a space shuttle," *IEEE Trans. Geosci. Remote Sens.*, vol. 43, no. 10, pp. 2315–2324, Oct. 2005.
[12] C. Buck, "An extension to the wide swath ocean altimeter concept," in *Proc. IEEE Int. Geosci. Remote Sens. Symp. (IGARSS)*, vol. 8. Jul. 2005, pp. 5436–5439.

[13] E. Rodriguez, D. Imel, and B. Houshmand, "Two-dimensional surface currents using vector along-track interferometry," in *Proc. PIERS*, 1995, p. 763.

[14] S. J. Frasier and A. J. Camps, "Dual-beam interferometry for ocean surface current vector mapping," *IEEE Trans. Geosci. Remote Sens.*, vol. 39, no. 2, pp. 401–414, Feb. 2001.

[15] J. V. Toporkov, D. Perkovic, G. Farquharson, M. A. Sletten, and S. J. Frasier, "Sea surface velocity vector retrieval using dual-beam interferometry: First demonstration," *IEEE Trans. Geosci. Remote Sens.*, vol. 43, no. 11, pp. 2494–2502, Nov. 2005.

[16] G. Farquharson, H. Deng, Y. Goncharenko, and J. Mower, "Dual-beam ATI SAR measurements of surface currents in the nearshore ocean," in *Proc. IEEE Int. Geosci. Remote Sens. Symp. (IGARSS)*, Jul. 2014, pp. 2661–2664.

[17] R. Bamler and P. Hartl, "Synthetic aperture radar interferometry," *Inverse Problems*, vol. 14, no. 4, pp. R1–R54, 1998.

[18] B. Chapron, F. Collard, and F. Ardhuin, "Direct measurements of ocean surface velocity from space: Interpretation and validation," *J. Geophys. Res. Oceans*, vol. 110, no. C7, p. C07008, Jul. 2005.

[19] J. A. Johannessen *et al.*, "Direct ocean surface velocity measurements from space: Improved quantitative interpretation of Envisat ASAR observations," *Geophys. Res. Lett.*, vol. 35, no. 22, p. L22608, Nov. 2008.

[20] D. R. Thompson and J. R. Jensen, "Synthetic aperture radar interferometry applied to ship-generated internal waves in the 1989 Loch Linnhe experiment," *J. Geophys. Res. Oceans*, vol. 98, no. C6, pp. 10259–10269, Jun. 1993.

[21] R. Romeiser and D. R. Thompson, "Numerical study on the along-track interferometric radar imaging mechanism of oceanic surface currents," *IEEE Trans. Geosci. Remote Sens.*, vol. 38, no. 1, pp. 446–458, Jan. 2000.

[22] V. Kudryavtsev, D. Akimov, J. Johannessen, and B. Chapron, "On radar imaging of current features: 1. Model and comparison with observations," *J. Geophys. Res. Oceans*, vol. 110, no. C7, p. C07016, Jul. 2005.

[23] R. Romeiser, "Current measurements by airborne along-track InSAR: Measuring technique and experimental results," *IEEE J. Ocean. Eng.*, vol. 30, no. 3, pp. 552–569, Jul. 2005.

[24] A. A. Mouche *et al.*, "On the use of Doppler shift for sea surface wind retrieval from SAR," *IEEE Trans. Geosci. Remote Sens.*, vol. 50, no. 7, pp. 2901–2909, Jul. 2012.

[25] A. C. H. Martin, C. Gommenginger, J. Marquez, S. Doody, V. Navarro, and C. Buck, "Wind-wave-induced velocity in ATI SAR ocean surface currents: First experimental evidence from an airborne campaign," *J. Geophys. Res. Oceans*, vol. 121, no. 3, pp. 1640–1653, Mar. 2016.

[26] A. Stoffelen and M. Portabella, "On Bayesian scatterometer wind inversion," *IEEE Trans. Geosci. Remote Sens.*, vol. 44, no. 6, pp. 1523–1533, Jun. 2006.

[27] P. W. Vachon and F. W. Dobson, "Validation of wind vector retrieval from ERS-1 SAR images over the ocean," *Global Atmos. Ocean Syst.*, vol. 5, no. 2, pp. 177–187, 1996.

[28] C. Gommenginger *et al.*, "Wavemill: A new mission for high-resolution mapping of total ocean surface current vectors," in *Proc. 10th Eur. Conf. Synth. Aperture Radar (EUSAR)*, Jun. 2014, pp. 1–4.

[29] C. Buck, C. Donlon, and N. Gebert, "A status update of investigations into the Wavemill concept," in *Proc. 10th Eur. Conf. Synth. Aperture Radar (EUSAR)*, Jun. 2014, pp. 1–4.

[30] M. W. Hansen, F. Collard, K. Dagestad, J. A. Johannessen, P. Fabry, and B. Chapron, "Retrieval of sea surface range velocities from Envisat ASAR Doppler centroid measurements," *IEEE Trans. Geosci. Remote Sens.*, vol. 49, no. 10, pp. 3582–3592, Oct. 2011.

[31] R. Romeiser *et al.*,"Direct surface current field imaging from space by along-track InSAR and conventional SAR,," in *Oceanography From Space, Revisited*, V. Barale, J. F. R. Gower, and L. Alberotanza, Eds. New York, NY, USA: Springer, 2010, pp. 73–91.

[32] K. Miller and M. Rochwarger, "A covariance approach to spectral moment estimation," *IEEE Trans. Inf. Theory*, vol. 18, no. 5, pp. 588–596, Sep. 1972.

[33] I. G. Cumming and F. H. Wong, *Digital Processing of Synthetic Apertur Radar Data: Algorithms and Implementation*. Norwood, MA, USA: Artech House, 2005.

[34] P. R. Kersten, J. V. Toporkov, T. L. Ainsworth, M. A. Sletten, and R. W. Jansen, "Estimating surface water speeds with a single-phase center SAR versus an along-track interferometric SAR," *IEEE Trans. Geosci. Remote Sens.*, vol. 48, no. 10, pp. 3638–3646, Oct. 2010.

[35] R. Romeiser, H. Runge, S. Suchandt, R. Kahle, C. Rossi, and P. S. Bell, "Quality assessment of surface current fields from TerraSAR-X and TanDEM-X along-track interferometry and Doppler centroid analysis," *IEEE Trans. Geosci. Remote Sens.*, vol. 52, no. 5, pp. 2759–2772, May 2014.

[36] P. López-Dekker, F. De Zan, T. Börner, G. Krieger, and A. Moreira, "Passive formation flying ATI-SAR for ocean currents observations: The PICOSAR concept," in *Proc. 1st Int. Earth Observ. Convoy Constellation Concepts Workshop (ESA-ESTEC)*, Noordwijk, The Netherlands, Oct. 2013, pp. 1–7.

[37] R. Romeiser and H. Runge, "Theoretical evaluation of several possible along-track InSAR modes of TerraSAR-X for ocean current measurements," *IEEE Trans. Geosci. Remote Sens.*, vol. 45, no. 1, pp. 21–35, Jan. 2007.

[38] M. J. Tucker, "The decorrelation time of microwave radar echoes from the sea surface," *Int. J. Remote Sens.*, vol. 6, no. 7, pp. 1075–1089, Jul. 1985.

[39] W. J. Pierson, Jr., and L. Moskowitz, "A proposed spectral form for fully developed wind seas based on the similarity theory of S. A. Kitaigorodskii," *J. Geophys. Res.*, vol. 69, no. 24, pp. 5181–5190, Dec. 1964.

[40] V. Kudryavtsev, D. Hauser, G. Caudal, and B. Chapron, "A semiempirical model of the normalized radar cross-section of the sea surface 1. Background model," *J. Geophys. Res. Oceans*, vol. 108, no. C3, p. 8054, Mar. 2003.

[41] V. N. Kudryavtsev, B. Chapron, A. G. Myasoedov, F. Collard, and J. A. Johannessen, "On dual co-polarized SAR measurements of the ocean surface," *IEEE Geosci. Remote Sens. Lett.*, vol. 10, no. 4, pp. 761–765, Jul. 2013.

[42] F. Saïd and H. Johnsen, "Ocean surface wind retrieval from dual-polarized SAR data using the polarization residual Doppler frequency," *IEEE Trans. Geosci. Remote Sens.*, vol. 52, no. 7, pp. 3980–3990, Jul. 2014.

[43] V. Kudryavtsev, I. Kozlov, B. Chapron, and J. A. Johannessen, "Quad-polarization SAR features of ocean currents," *J. Geophys. Res. Oceans*, vol. 119, no. 9, pp. 6046–6065, Sep. 2014.

[44] S. H. Yueh, W. J. Wilson, and S. Dinardo, "Polarimetric radar remote sensing of ocean surface wind," *IEEE Trans. Geosci. Remote Sens.*, vol. 40, no. 4, pp. 793–800, Apr. 2002.

[45] R. K. Raney, "Hybrid-polarity SAR architecture," *IEEE Trans. Geosci. Remote Sens.*, vol. 45, no. 11, pp. 3397–3404, Nov. 2007.

[46] M. S. Seymour and I. G. Cumming, "Maximum likelihood estimation for SAR interferometry," in *Proc. Geosci. Remote Sens. Symp. (IGARSS) Surface Atmos. Remote Sens. Technol. Data Anal. Interpretation Int.*, vol. 4, Aug. 1994, pp. 2272–2275.

[47] D. Moller, B. Pollard, and E. Rodriguez, "Feasibility study and system design for a spaceborne along-track interferometer/scatterometer," in *Proc. AIRSAR Earth Sci. Appl. Workshop*, Pasadena, CA, USA, Mar. 2002, pp. 1–9.

[48] E. Rodriguez and J. M. Martin, "Theory and design of interferometric synthetic aperture radars," *IEE Proc. F Radar Signal Process.*, vol. 139, no. 2, pp. 147–159, Apr. 1992.

[49] J.-S. Lee, K. W. Hoppel, S. A. Mango, and A. R. Miller, "Intensity and phase statistics of multilook polarimetric and interferometric SAR imagery," *IEEE Trans. Geosci. Remote Sens.*, vol. 32, no. 5, pp. 1017–1028, Sep. 1994.

[50] B. Kinsman, *Wind Waves: Their Generation and Propagation on the Ocean Surface*. North Chelmsford, MA, USA: Courier Corporation, 1965.

[51] R. D. Chapman, B. L. Gotwols, and R. E. Sterner, "On the statistics of the phase of microwave backscatter from the ocean surface," *J. Geophys. Res. Oceans*, vol. 99, no. C8, pp. 16293–16301, Aug. 1994.

[52] S. Watts, "Radar sea clutter: Recent progress and future challenges," in *Proc. Int. Conf. Radar*, Sep. 2008, pp. 10–16.

[53] K. Hasselmann *et al.*, "Theory of synthetic aperture radar ocean imaging: A MARSEN view," *J. Geophys. Res. Oceans*, vol. 90, no. C3, pp. 4659–4686, May 1985.

[54] K. D. Ward, R. Tough, and S. Watts, *Sea Clutter: Scattering, the K Distribution and Radar Performance*. London, U.K.: The Institution of Engineering and Technology, Jun. 2006.

[55] K. D. Ward, "Compound representation of high resolution sea clutter," *Electron. Lett.*, vol. 17, no. 16, pp. 561–563, Aug. 1981.

[56] D. J. Crisp, L. Rosenberg, N. J. Stacy, and Y. Dong, "Modelling X-band sea clutter with the K-distribution: Shape parameter variation," in *Proc. Int. Radar Conf. Surveillance Safer World (RADAR)*, Oct. 2009, pp. 1–6.

[57] P. López-Dekker. (Mar. 2017). *Simple Numerical Analysis of the Multi-Looked Interferometric Phase Error for K-Distributed Signals*. [Online]. Available: https://www.codeocean.com/ and https://codeocean.com/2017/03/02/simple-numerical-analysis-of-the-multi-looked-interferometric-phase-error-for-k-distributed-signals/

[58] F. J. Wentz and D. K. Smith, "A model function for the ocean-normalized radar cross section at 14 GHz derived from NSCAT observations," *J. Geophys. Res. Oceans*, vol. 104, no. C5, pp. 11499–11514, May 1999.

[59] W. L. Jones *et al.*, "The SEASAT-A satellite scatterometer: The geophysical evaluation of remotely sensed wind vectors over the ocean," *J. Geophys. Res. Oceans*, vol. 87, no. C5, pp. 3297–3317, Apr. 1982.

[60] G. Krieger, K. P. Papathanassiou, and S. R. Cloude, "Spaceborne polarimetric SAR interferometry: Performance analysis and mission concepts," *EURASIP J. Adv. Signal Process.*, vol. 2005, no. 20, p. 354018, Dec. 2005.

[61] I. Young, "Seasonal variability of the global ocean wind and wave climate," *Int. J. Climatol.*, vol. 19, no. 9, pp. 931–950, Jul. 1999.

[62] S. Wollstadt *et al.*, "A ku-band SAR mission concept for ocean surface current measurement using dual beam ATI and hybrid polarization," in *Proc. IEEE Int. Geosci. Remote Sens. Symp. (IGARSS)*, Jul. 2015, pp. 1219–1222.

[63] P. López-Dekker *et al.*, "A ku-band ATI SAR mission for total ocean surface current vector retrieval: System concept and performance," in *Proc. Adv. RF Sensors Remote Sens. Instrum. Workshop (ARSI) (ESA-ESTEC)*, Noordwijk, The Netherlands, Nov. 2014, pp. 1–8.

[64] M. Süess, B. Grafmüller, and R. Zahn, "A novel high resolution, wide swath SAR system," in *Proc. Int. Geosci. Remote Sens. Symp. (IGARSS)*, vol. 3. Sydney, Australia, Jul. 2001, pp. 1013–1015.

[65] M. Süß and W. Wiesbeck, "Side-looking synthetic aperture radar system," European Patent EP 1 241 487, Sep. 12, 2002.

Steffen Wollstadt received the Dipl.Ing. (M.Sc.) degree in electrical engineering from the Technical University of Darmstadt, Darmstadt, Germany, in 2005, with a thesis on metamaterial-based microstrip antenna design.

In 2006, he joined the Microwaves and Radar Institute, German Aerospace Center (DLR), Oberpfaffenhofen, Germany. Until 2008, he was with the Satellite Synthetic Aperture Radar (SAR) Systems Department, as a Project Engineer in the System Engineering and Calibration part of the TerraSAR-X ground segment, where he was involved in the TerraSAR-X and TanDEM-X instrument command generation. Since 2009, he has been with the SAR Missions Research Group, Radar Concepts Department, where he has been involved in TOPS Sentinel-1 image quality and SAR performance investigations and in various experiments with TerraSAR-X and TanDEM-X about novel imaging modes and SAR performance improvement. He is responsible for the commanding of experimental TOPS imaging mode acquisitions with TerraSAR-X. His research interests include spaceborne SAR mission and instrument analysis and interferometric problems, including along-track, repeat-pass, and differential interferometry.

Paco López-Dekker (S'98–M'03–SM'14) was born in Nijmegen, The Netherlands, in 1972. He received the Ingeniero degree in telecommunication engineering from the Universitat Politècnica de Catalunya (UPC), Barcelona, Spain, in 1997, the M.S. degree in electrical and computer engineering from the University of California at Irvine, Irvine, CA, USA, in 1998, under the Balsells Fellowship, and the Ph.D. degree from the University of Massachusetts, Amherst, MA, USA, in 2003, for his research on clear-air imaging radar systems to study the atmospheric boundary layer.

From 1999 to 2003, he was with the Microwave Remote Sensing Laboratory, University of Massachusetts. In 2003, he was with Starlab, Barcelona, Spain, where he was involved in the development of GNSS-R sensors. From 2004 to 2006, he was a Visiting Professor with the Department of Telecommunications and Systems Engineering, Universitat Autònoma de Barcelona, Barcelona. In 2006, he joined the Remote Sensing Laboratory, UPC, where he conducted research on bistatic synthetic aperture radar (SAR) under a five-year Ramon y Cajal Grant. He taught courses on signals and systems, signal processing, communications systems and radiation, and guided waves at UPC. From 2009 to 2016, he led the SAR Missions Group, Microwaves and Radar Institute, German Aerospace Center (DLR), Oberpfaffenhofen, Germany. The focus of the group was the study of future SAR missions, including the development of novel mission concepts and detailed mission performance analyses. Since 2016, he has been an Associate Professor with the Faculty of Civil Engineering and Geosciences, Delft University of Technology, Delft, The Netherlands.

Francesco De Zan received the master's degree in telecommunication engineering and the Ph.D. degree with a thesis on synthetic aperture radar (SAR) interferometry and decorrelating targets from the Politecnico di Milano, Milan, Italy, in 2004 and 2008, respectively.

He has collaborated with T.R.E., Milan, Italy, on persistent scatterer interferometry and with the European Space Agency, Noordwijk, The Netherlands, about the Interferometric Wide Swath Mode of the Sentinel-1 Mission. In 2007, he visited for six months the Stanford Exploration Project at Stanford University, Stanford, CA, USA. He has been with the German Aerospace Center (DLR), Oberpfaffenhofen, Germany, since 2008, first at the Microwaves and Radar Institute, then at the Remote Sensing Technology Institute. His research interests include modeling and performance analysis of future SAR missions, algorithm development for SAR interferometry, and the interferometric/radargrammetric calibration of existing instruments (TanDEM-X, Sentinel-1).

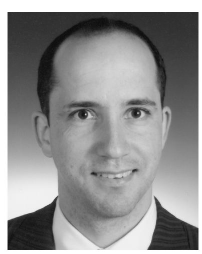

Marwan Younis (S'95–M'05–SM'08) received the B.Sc. degree in electrical engineering from the University of Baghdad, Baghdad, Iraq, in 1992, and the Dipl.Ing. (M.Sc.) and Dr.-Ing. (Ph.D.) degrees in electrical engineering from the Universität Karlsruhe (TH), Karlsruhe, Germany, in 1997 and 2004, respectively.

In 1996, he was an Intern with the Jet Propulsion Laboratory, Pasadena, CA, USA, where he spent a three month research sabbatical in 2013. From 1998 to 2004, he was a Research Scientist with the Institut für Höchstfrequenztechnik und Elektronik, TH. Since 2005, he has been with the Microwaves and Radar Institute, German Aerospace Center (DLR), Oberpfaffenhofen, Germany. He is currently a Lecturer with the Karlsruhe Institute of Technology, Karlsruhe, and also with Carl-Cranz-Gesellschaft, Wessling, Germany. He has authored or co-authored about 150 conference papers, and 30 reviewed publications. His research interests include synthetic aperture radar (SAR) systems and techniques, MIMO SAR, digital beamforming, SAR performance, calibration, and antennas.

Dr. Younis received the Hermann-Billing Award for his Ph.D. thesis in 2005. He is the Co-Chair of the Instrumentation and Future Technologies GRSS Technical Committee. He is also an Associate Editor of the IEEE GEOSCIENCE AND REMOTE SENSING LETTERS and a Reviewer of the IEEE publications.